Article

Macrophage-derived insulin antagonist *ImpL2* induces lipoprotein mobilization upon bacterial infection

Gabriela Krejčová[1] (iD), Cecilia Morgantini[2], Helena Zemanová[1], Volker M Lauschke[2,3,4],
Julie Kovářová[5] (iD), Jiří Kubásek[6], Pavla Nedbalová[1], Nick Kamps-Hughes[7], Martin Moos[8],
Myriam Aouadi[2], Tomáš Doležal[1,*] (iD) & Adam Bajgar[1,**] (iD)

Abstract

The immune response is an energy-demanding process that must be coordinated with systemic metabolic changes redirecting nutrients from stores to the immune system. Although this interplay is fundamental for the function of the immune system, the underlying mechanisms remain elusive. Our data show that the pro-inflammatory polarization of *Drosophila* macrophages is coupled to the production of the insulin antagonist *ImpL2* through the activity of the transcription factor HIF1α. *ImpL2* production, reflecting nutritional demands of activated macrophages, subsequently impairs insulin signaling in the fat body, thereby triggering FOXO-driven mobilization of lipoproteins. This metabolic adaptation is fundamental for the function of the immune system and an individual's resistance to infection. We demonstrated that analogically to *Drosophila*, mammalian immune-activated macrophages produce *ImpL2* homolog IGFBP7 in a HIF1α-dependent manner and that enhanced IGFBP7 production by these cells induces mobilization of lipoproteins from hepatocytes. Hence, the production of *ImpL2*/IGFBP7 by macrophages represents an evolutionarily conserved mechanism by which macrophages alleviate insulin signaling in the central metabolic organ to secure nutrients necessary for their function upon bacterial infection.

Introduction

Rapid activation of the mononuclear phagocytic system is critical for limiting bacterial burden and promoting resistance to infection (Chow *et al*, 2011). However, the activation of the immune system is an energetically and nutritionally demanding process requiring a coordinated response of almost all organs and tissues within the organism (Rankin & Artis, 2018). Although metabolic reprogramming accompanies virtually any immune response and can profoundly affect patient health (Chi, 2022), the mechanism coordinating the immune response with systemic metabolism remains poorly understood.

Upon recognition of a pathogen, macrophages adopt a pro-inflammatory polarization to enhance their bactericidal capacity and secrete pro-inflammatory cytokines that propagate information about the pathogenic threat to other tissue in the body (Mills *et al*, 2000). This polarization is achieved by stabilizing the transcription factor HIF1α that governs the complex rewiring of macrophage cellular metabolism, which is generally referred to as aerobic glycolysis (Galvan-Pena & O'Neill, 2014). However, this metabolic adaptation leads to the rapid depletion of macrophage intracellular stores and makes them functionally dependent on external sources of nutrients (Ganeshan & Chawla, 2014).

Along with the rewiring of the cellular metabolism of the immune cells, systemic metabolism also exhibits substantial adjustments. For example, altered hormonal signaling, and subsequent disruption of metabolic homeostasis manifested by loss of nutritional stores and their enhanced level in circulation (hyperglycemia, hyperlipidemia), are commonly observed accompanying signs in patients suffering from severe bacterial infections (Wasyluk & Zwolak, 2021).

Recently, insulin resistance has been considered an adaptive mechanism of energy redistribution during acute metabolic stress

1 Department of Molecular Biology and Genetics, Faculty of Science, University of South Bohemia, Ceske Budejovice, Czech Republic
2 Department of Medicine, Integrated Cardio Metabolic Center (ICMC), Karolinska Institutet, Huddinge, Sweden
3 Dr Margarete Fischer-Bosch Institute of Clinical Pharmacology, Stuttgart, Germany
4 University of Tübingen, Tübingen, Germany
5 Biology Centre CAS, Institute of Parasitology, Ceske Budejovice, Czech Republic
6 Department of Experimental Plant Biology, Faculty of Science, University of South Bohemia, Ceske Budejovice, Czech Republic
7 Institute of Molecular Biology, University of Oregon, Oregon City, OR, USA
8 Institute of Entomology, Biology Centre CAS, Ceske Budejovice, Czech Republic
*Corresponding author. Tel: +420 384 772 229; E-mail: tomas.dolezal@prf.jcu.cz
**Corresponding author. Tel: +420 774 912 172; E-mail: bajgaradam@seznam.cz; bajgaa00@prf.jcu.cz

(Tsatsoulis *et al*, 2013). However, this concept is in stark contrast to the common perception of insulin resistance as a pathological process associated with obesity, atherosclerosis, arthritis, and cachexia (Akhtar *et al*, 2019), and the possible adaptive role of insulin resistance has been neglected so far. Interestingly, the increased production of pro-inflammatory cytokines by the activated immune system plays a central role in the induction of insulin resistance and the progression of the diseases mentioned above (Al-Mansoori *et al*, 2022).

In this work, we aim to investigate the factors inducing the mobilization of nutrients required to supplement the nutritional demands of the activated immune system.

To reveal the role of macrophages in the regulation of systemic metabolism during the immune response, we employed an established experimental model of streptococcal infection in *Drosophila* (Bajgar & Dolezal, 2018). Exploiting this experimental system, we have previously demonstrated that *Drosophila* macrophages undergo pro-inflammatory polarization in response to bacterial infection associated with HIF1α-driven aerobic glycolysis in a manner analogous to that observed in mammals (Krejčová *et al*, 2019). Moreover, streptococcal infection in this model is accompanied by substantial remodeling of systemic carbohydrate and lipid metabolism (Dionne & Schneider, 2008; Bajgar & Dolezal, 2018).

Here we demonstrate that pro-inflammatory macrophage polarization is coupled with the production of the signaling factor IMPL2, which alleviates insulin signaling in the central metabolic organ of flies, the fat body. Macrophage-derived IMPL2 is required for the mobilization of lipid stores in the form of lipoproteins, which is fundamental for the nutritional supplementation of bactericidal macrophages and resistance to infection. Our data further imply that this mechanism is evolutionarily conserved in mammals. Indeed, mammalian macrophages produce the mammalian *ImpL2* homolog *Insulin growth factor binding protein 7* (*IGFBP7*), which induces the mobilization of lipoproteins from hepatocytes during bacterial infection.

Results

Infection leads to systemic redistribution of lipids

To elicit an immune response, adult fruit flies (*Drosophila melanogaster*) were injected with 20,000 extracellular bacteria (*Streptococcus pneumoniae*). In our experimental model, acute streptococcal infection leads to rapid activation of macrophages, called plasmatocytes in *Drosophila*, and their pro-inflammatory polarization (Bajgar & Dolezal, 2018; Krejčová *et al*, 2019). The infection culminates during the first 24 h of infection, which determines whether or not an individual survives the infection. Although all pathogenic bacteria in surviving flies are eliminated within the first 5 days, the flies continue to decline due to the long-term effects of the infection experienced (Bajgar & Dolezal, 2018; Krejčová *et al*, 2019). This treatment offers a standardized course of immune response in which macrophage pro-inflammatory polarization and their bactericidal activity is crucial for limiting the bacterial burden (Bajgar & Dolezal, 2018). To determine how the ongoing immune response is reflected by rearrangement of the systemic metabolism, we analyzed metabolic changes in infected individuals 24 h post-infection (hpi).

We found that the acute phase of infection is accompanied by a depletion of two major storage molecules, glycogen (GLY) and triglycerides (TG) when measured on the whole-individual level (Fig 1A). This is consistent with the pattern observed in the fat body, organ comprising the functionalities of mammalian liver and adipose tissue. In this tissue, the levels of all analyzed carbohydrates and lipids are significantly reduced upon infection (Fig 1B). Depletion of lipid stores is further documented by a significantly decreased diameter of lipid droplets and the area they occupy in adipocytes of infected flies (Fig 1C) as quantified from the confocal images of the fat body stained for neutral lipids (Fig 1D).

Examination of the fat body lipid content using lipidomic analysis revealed that depletion of lipid stores in this organ is accompanied by a significant shift in lipid composition. While the main storage lipids, triglycerides, prevail in the fat body of control flies, their relative amounts decrease significantly after infection in favor of polar lipids (phosphatidylcholine, PC; phosphatidylethanolamine, PE) and diglycerides (DG; Figs 1E and EV1A), a transport form of lipids in insects (Palm *et al*, 2012).

Contrary to that, the titer of carbohydrates and lipids rises significantly in circulation upon infection (Fig 1F). These observations imply that the infection is accompanied by depletion of energy stores and redistribution of nutrients between tissues via circulation. To investigate whether mobilized nutrients serve as metabolic support for the activated immune system, we analyzed the metabolic profile of macrophages at 24 hpi. Macrophages isolated from infected individuals display elevated levels of all analyzed carbohydrates and lipids when compared to uninfected controls (Fig 1G).

Lipidomic analysis revealed that the overall lipid content is 3.5-fold increased in infection-activated macrophages compared to controls (Fig EV1B). Moreover, the infection affects the lipid composition in these cells displaying a significantly enhanced fraction of hydrolyzed forms of polar lipids (lysophosphatidylcholine, LPC; lysophosphatidylethanolamine, LPE; Figs 1H and EV1C) that may be attributed to increased endocytosis of circulating lipoproteins and eicosanoid production (Lee *et al*, 2020; Liu *et al*, 2020).

To further characterize the infection-induced redistribution of lipids from the fat body to macrophages, we fed flies with a mixture of ^{13}C-labeled free fatty acids (^{13}C-FFAs) and monitored their immediate incorporation into tissues. While in control subjects, most of the ^{13}C-FFAs are destined for the fat body, and only a small fraction incorporates into macrophages, this ratio is completely reversed upon infection (Fig 1I). Since the control and infected flies display comparable dietary intake, the possibility that the observed differences may be accounted to infection-induced anorexia can be excluded (Fig EV1D). Overall, our data show that infection is accompanied by a rearrangement of systemic metabolism that leads to a redistribution of lipids from the central metabolic organ toward the circulation and the activated immune system. To explore the possibility that the observed metabolic changes are induced by signaling factors originating from macrophages, we proceeded to a detailed analysis of these cells after infection (Fig 1J).

Infection-activated macrophages increase *ImpL2* expression in a HIF-1α-dependent manner

To better understand the ongoing processes in infection-activated macrophages, we performed a comparative analysis of their
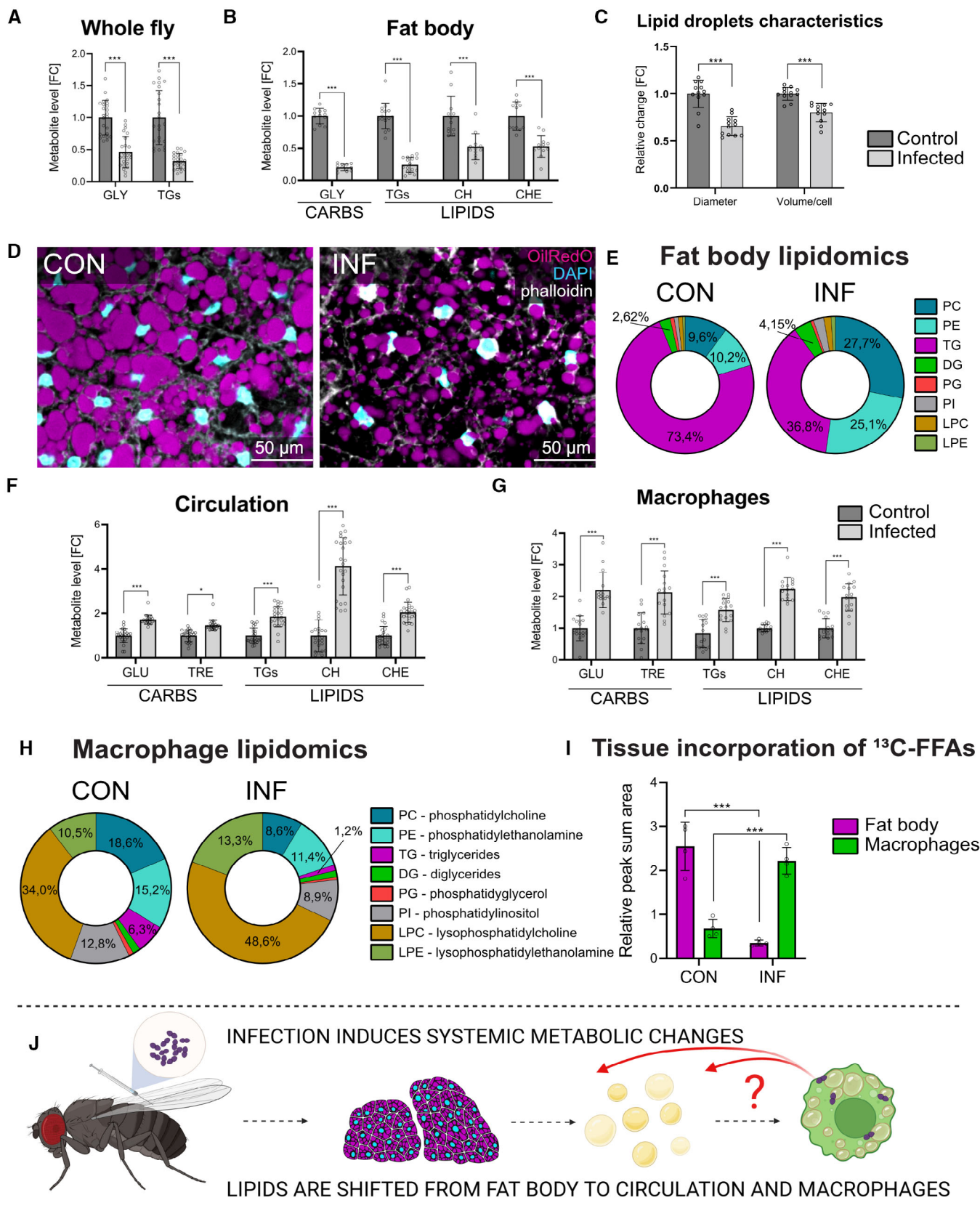
Figure 1.

◀

Figure 1. Infection leads to systemic redistribution of lipids.

A   Whole body amounts of glycogen (GLY) and triglycerides (TG) after infection, expressed as fold change in infected flies compared to control.
B   The level of glycogen (GLY) and lipids (CH, cholesterol; CHE, cholesteryl-ester; TGs, triglycerides) in the fat body after infection, expressed as fold change in infected flies compared to controls.
C   Lipid droplet diameter and volume of lipid droplets per adipocyte in the fat body expressed as fold change in infected flies compared to controls. Data were obtained from the quantification of lipid droplet characteristics in confocal images of dissected fat body tissues (shown in D).
D   Representative confocal images documenting the morphology of lipid droplets in the fat body whole mounts of control (CON) and infected (INF) flies. Lipids stained by OilRedO (magenta); DAPI (cyan) labels nuclei; membranes stained by phalloidin (white).
E   Lipidomic analysis showing the proportional change in lipid species in the fat body dissected from control (CON) and infected (INF) flies. Samples were collected in six independent experiments; data was expressed as a percent of the total amount of lipids in the sample.
F   A titer of carbohydrates (GLU, glucose; TRE, trehalose) and lipids (CH, cholesterol; CHE, cholesteryl-ester; TGs, triglycerides) in the circulation after infection, expressed as fold change in infected flies compared to controls.
G   The amounts of carbohydrates (GLU, glucose; TRE, trehalose) and lipids (CH, cholesterol; CHE, cholesteryl-ester; TGs, triglycerides) in macrophages after infection, expressed as fold change in infected flies compared to control.
H   Lipidomics analysis showing the proportional change in lipid species in macrophages isolated from control (CON) and infected (INF) flies. In five biological replicates; normalized to the number of isolated cells.
I   Incorporation of dietary ^{13}C-labeled free fatty acids into the fat body and macrophages in control (CON) and infected (INF) flies, expressed as relative incorporation of ^{13}C free fatty acids normalized to ^{12}C free fatty acids in the sample.
J   Schematic representation of the results obtained. Infection leads to a systemic redistribution of lipids in the body, indicating a mobilization of resources to be available for the immune response. The role of potential macrophage-derived signaling factors in this process is unknown.

Data information: Fat bodies from six individuals and macrophages from 160 flies were used for each biological replicate. The plots display data obtained 24 h post-infection. For (A–C, F and G), data are reported as fold change relative to controls arbitrarily set to 1. Metabolite concentrations in A, B, F and H were normalized to protein level in the sample. For analysis of metabolites; six whole flies, fat bodies from six individuals, hemolymph from 25 flies, and macrophages from 160 flies were used for each biological replicate. For lipidomic analysis; fat bodies from six individuals and macrophages from 300 flies were used for each biological replicate. Individual dots in the plots represent biological replicates. Samples for lipidomics were obtained in five biological replicates for macrophages and in six biological replicates for the fat bodies. Results were compared by 2way ANOVA followed by Šídák's multiple comparisons test. Values are displayed as mean ± SD, asterisks mark statistically significant differences (*$P < 0.05$; ***$P < 0.001$).
Source data are available online for this figure.

transcriptomic profile at 24 hpi. Gene set enrichment analysis revealed that along with the activation of immune-related processes, macrophages undergo remarkable changes in their cellular metabolism (Figs 2A and EV2A). Infection-activated macrophages attenuate the expression of genes involved in the mitochondrial generation of ATP and simultaneously enhance the expression of genes involved in the regulation of lipid and cholesterol metabolism (Fig 2A). These data further extend our previous observations that bactericidal polarization of *Drosophila* macrophages is coupled with the remodeling of their cellular metabolism toward aerobic glycolysis (Krejčová *et al*, 2019). We have previously shown that the adoption of aerobic glycolysis by *Drosophila* macrophages is fundamental for their bactericidal function and that this metabolic remodeling is analogical to mammalian macrophages governed by the master regulator *Hif1α*, which controls the expression of many metabolic genes (Galvan-Pena & O'Neill, 2014; Krejčová *et al*, 2019).

We further identified several signaling factors whose induction goes hand in hand with infection-induced macrophage polarization (Fig 2B). From several candidates, we chose *ImpL2* for further investigation since it is highly expressed in macrophages, displays the most significant increase in response to infection (Figs 2C and EV2B), and has been previously shown to have a potential to affect systemic lipid metabolism (Kwon *et al*, 2015). Other potential candidates, the signaling factors *Unpaired 3* (*Upd3*) and *Eiger* (*Egr*) were tested together with *ImpL2*, but already the initial experiments showed that neither *Upd3* nor *Egr* had a rather negligible effect on lipid mobilization from the fat body during infection (Appendix Figs S1–S6).

To investigate the spatial pattern of *ImpL2* expression, we employed a fly strain bearing a fluorescent *ImpL2* reporter (*ImpL2-Gal4 > UASmCherry*). We found that *ImpL2* promoter activity is almost exclusive to macrophages, as evidenced by the strong production of the *ImpL2-mCherry* signal in cells positive for the *Drosophila* macrophage marker NimC1 (Fig 2D and Appendix Fig S7).

Next, we investigated the mechanism controlling *ImpL2* expression in these cells. Given that HIF1α is the master regulator of macrophage metabolic remodeling during infection, we assessed its effect on *ImpL2* expression. Macrophage-specific knockdown of *Hif1α* (*Crq > Gal4*; *UAS-GFP, Hif1α^RNAi*) abolished the infection-induced increase in *ImpL2* expression in these cells (Fig 2E; see Fig EV2C for *Hif1α^RNAi* efficiency; see Fig EV2D for genotype explanations). This interaction is further confirmed by the direct binding of HIF1α to the *ImpL2* promoter, as revealed by Chip-qPCR analysis (Fig 2F).

Taken together, the presented data show that metabolic rearrangement of pro-inflammatory macrophages is coupled to *ImpL2* expression since both processes are governed by the same transcription factor, HIF1α. This implies a possible role of *ImpL2* as a signal produced by pro-inflammatory macrophages in reflection of their newly adopted metabolic program associated with specific nutritional demands (Fig 2G).

Macrophage-derived IMPL2 directs the infection-induced mobilization of lipid stores

To investigate the effect of macrophage-derived IMPL2 on the redistribution of lipids during infection, we generated flies carrying genetic constructs for time-limited macrophage-specific *ImpL2* knockdown (Mφ-*ImpL2^RNAi*) or overexpression (Mφ-*ImpL2^CDS*). Using these fly strains, we experimentally manipulated *ImpL2* expression macrophage-specifically 24 h before the infection and compared the effect of these interventions to control lines of the
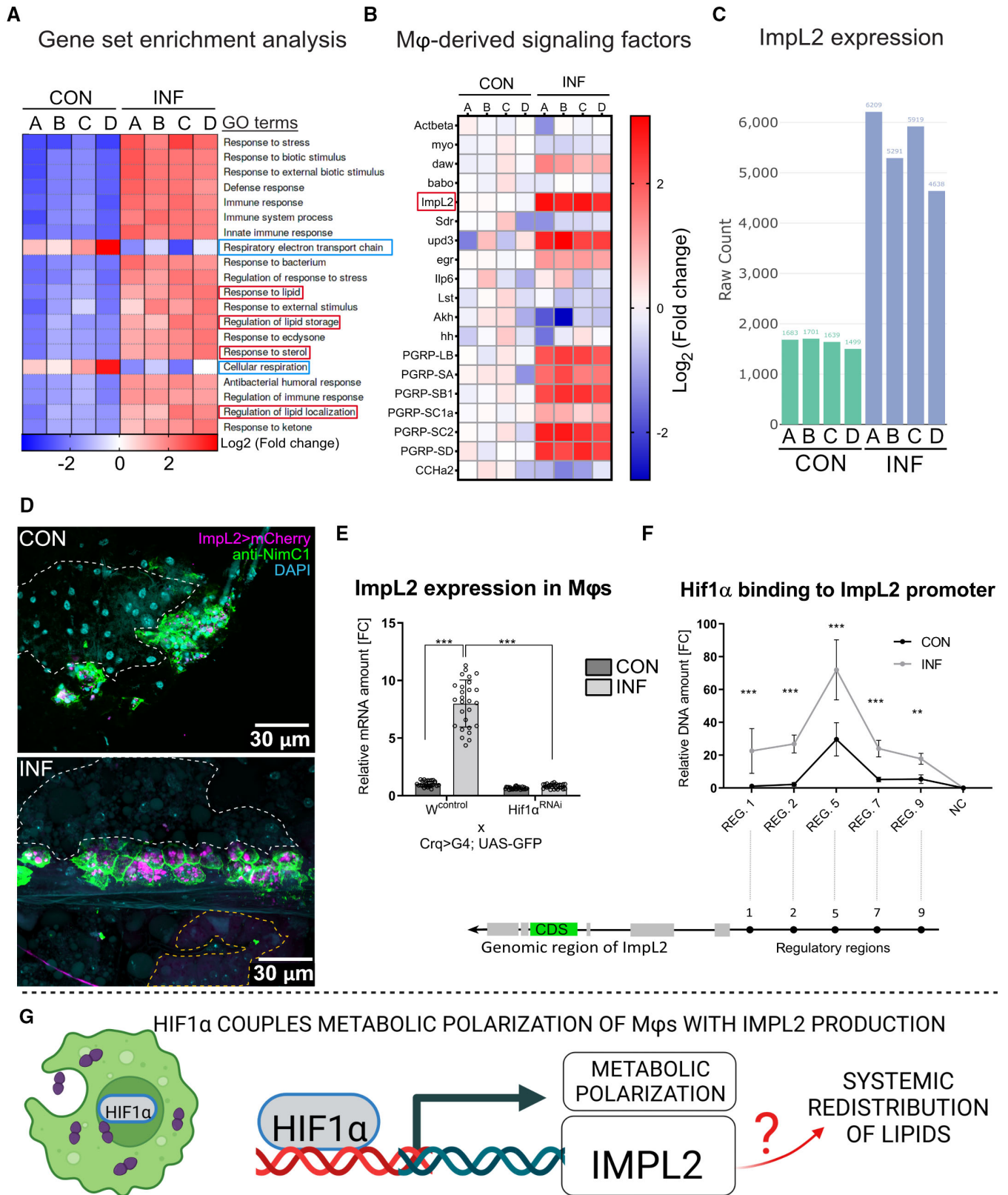
A Gene set enrichment analysis

B Mφ-derived signaling factors

C ImpL2 expression

D

E ImpL2 expression in Mφs

F Hif1α binding to ImpL2 promoter

G HIF1α COUPLES METABOLIC POLARIZATION OF Mφs WITH IMPL2 PRODUCTION

Figure 2.

◀

Figure 2. Infection-activated macrophages increase the *ImpL2* expression in a *Hif1α*-dependent manner.

A   Gene set enrichment analysis of transcriptomic data from macrophages isolated from infected flies (INF) compared to controls (CON). Heat map displays the top 20 significantly altered gene sets, Gene Ontology (GO) terms retrieved from KEGG pathways. Silenced mitochondrial respiration (blue rectangles) and upregulation of lipid-related pathways (red rectangles) are highlighted.

B   Heat map documenting the differential expression of secreted signaling factors in macrophages isolated from infected individuals (INF) compared to controls (CON), expressed as Log_2 fold change in infected flies compared to control.

C   Expression level of *ImpL2* in macrophages isolated from infected individuals compared to controls, data presented as raw count level (counts per million).

D   Representative confocal microscopy images of abdominal whole mounts, illustrating *ImpL2* expression (*ImpL2>mCherry*; magenta) in macrophages (stained by an anti-NimC1 antibody; green) of control and infected flies compared to the surrounding tissues (fat body, white dashed line; oenocytes, yellow dashed line). Nuclei stained by DAPI (cyan). From Z-stack consisting of a maximum projection of 11 layers.

E   Expression of *ImpL2* in macrophages isolated from infected (INF) and control (CON) in flies with macrophage-specific *Hif1α* knockdown (*Hif1α^RNAi*) and their respective control (*W^control*). Expression levels normalized against rp49 are reported as fold change relative to *ImpL2* levels in uninfected *W^control* flies arbitrarily set to 1. *Results compared by 2way ANOVA Tukey's multiple comparisons test.*

F   ChiP-qPCR analysis showing the abundance of arbitrarily preselected regions in *ImpL2* promoter bound by the transcription factor HIF1α in control (CON) and infected flies (INF). The genomic region of *S-adenosylmethionin synthetase* with no predicted HIF1α-binding sites was used as a negative control (NC). Data normalized to the number of detected fragments in the slurry before chromatin immunoprecipitation. Data are reported as fold change relative to REG.1 level in uninfected *W^control* flies arbitrarily set to 1. *Results compared by 2way ANOVA Šídák's multiple comparisons test.*

G   Schematic representation of the obtained results. The transcription factor HIF1α binds to the *ImpL2* promoter to increase its expression in macrophages after infection. Thus, *ImpL2* production is coupled to the metabolic polarization of pro-inflammatory macrophages toward aerobic glycolysis via HIF1α activity. Whether macrophage-derived IMPL2 induces systemic lipid redistribution will be addressed in the following sections.

Data information: All data presented in this figure were obtained 24 h post-infection. Data were obtained from four independent experiments if not stated otherwise. For qPCR analysis, the dots in the plots represent biological replicates. For transcriptomic analysis, macrophages from 300 flies were used for each biological replicate. For qPCR analysis, macrophages from 90 flies were used for each biological replicate. Values are displayed as mean ± SD, asterisks mark statistically significant differences (**$P < 0.01$; ***$P < 0.001$).

Source data are available online for this figure.

respective genetic background (*TRiP^control*, *W^control*; see Fig EV2D for an explanation of the genotypes and Fig EV3A for efficiency of macrophages-specific *ImpL2* manipulations).

First, we evaluated the impact of Mφ-*ImpL2* manipulations on the morphology of the fat body. While flies of the control genotypes (*TRiP^control*, *W^control*) display the characteristic infection-induced changes in the morphology of lipid droplets in adipocytes, Mφ-*ImpL2^RNAi* abrogates these changes. Accordingly, macrophage-specific overexpression of *ImpL2* (Mφ-*ImpL2^CDS*) is sufficient to mimic the infection-induced changes even under control conditions (Figs 3A and EV3B and C). These morphological changes can be attributed to the redistribution of lipids from the fat body to the circulation, as evidenced by triglyceride, cholesterol, and cholesteryl-ester levels, which are decreased in the fat body and elevated in circulation upon infection. Since all these metabolites show an identical pattern in response to treatments and genetic manipulations, they are displayed in the main Figures as "Lipids" for simplicity and presented individually in the Expanded View file (Fig EV3D–F).

While Mφ-*ImpL2^RNAi* prevents the infection-induced depletion of lipids in the fat body and their subsequent rise in circulation, these changes are invoked by mere Mφ-*ImpL2^CDS* even without infection (Figs 3B and C, and EV3D–F).

Fat body lipidomics provides further indications that macrophage-derived IMPL2 plays a central role in the mobilization of lipids upon infection. Mφ-*ImpL2^RNAi* suppresses the characteristic infection-induced changes in the proportion of lipid species in the fat body as manifested by increased abundance of PC, PE, and DG, whereas enrichment of these lipid classes can be observed in the fat body of flies carrying Mφ-*ImpL2^CDS* even under control conditions (Fig 3D and E).

To comprehend the mechanism of the *ImpL2*-induced changes in the fat body, we measured the expression pattern of genes involved in lipolysis (*brummer*, *bmm*; *Hormone-sensitive lipase*, *Hsl*) and the production of lipoproteins (*Apolipoprotein lipid transfer particle*, *Apoltp*; *apolipophorin*, *apolpp*; *Neuropeptide-like precursor 2*, *Nplp2*;

Microsomal triacylglycerol transfer protein, *Mtp*). Expression of all these genes is significantly elevated in the fat body upon infection, and the expression pattern of *bmm*, *Apoltp*, *apolpp*, and *Mtp* seems to be dependent on macrophage-derived *ImpL2* (Figs 3F and EV4A). Interestingly, all these genes are known FOXO targets (Brankatschk *et al*, 2014), which implicates the involvement of this transcription factor in the mediation of IMPL2 effects. This notion is supported by the expression of two commonly used FOXO readouts (*Thor*, *4EBP*; *eukaryotic translation initiation factor 4E1*, *eIF4E1*; Santalla *et al*, 2022), showing analogous expression patterns with respect to infection and Mφ-*ImpL2* manipulations (Fig 3F). Consistent with metabolic effects attributed to Mφ-*ImpL2* manipulations, identical metabolic effect has been achieved also by using an alternative *ImpL2^RNAi* fly line (Appendix Figs S16–S18). Infection also leads to increased expression of *Hsl* and the exchange lipoprotein *Nplp2* in the fat body, however, their expression is not affected by Mφ-*ImpL2* manipulations, suggesting an alternative mechanism for their regulation.

Macrophage-derived IMPL2 drives lipid mobilization via alleviation of fat body insulin signaling

To determine whether FOXO plays a role in the manifestation of IMPL2 effects in the fat body, we decided to analyze its subcellular localization and its contribution to the infection-induced changes in lipid droplet morphology. While FOXO may be found distributed evenly between the nucleus and cytosol under normal physiological conditions, it becomes predominantly nuclear in response to metabolic stress (Koyama *et al*, 2014). This translocation also occurs during bacterial infection; however, it is impaired by Mφ-*ImpL2^RNAi* and can be induced by Mφ-*ImpL2^CDS* even in uninfected individuals (Figs 4A and EV5A). Moreover, flies carrying the hypomorphic *foxo* allele together with Mφ-*ImpL2^CDS* do not exhibit lipid depletion observed otherwise in Mφ-*ImpL2^CDS* flies, as documented by lipid
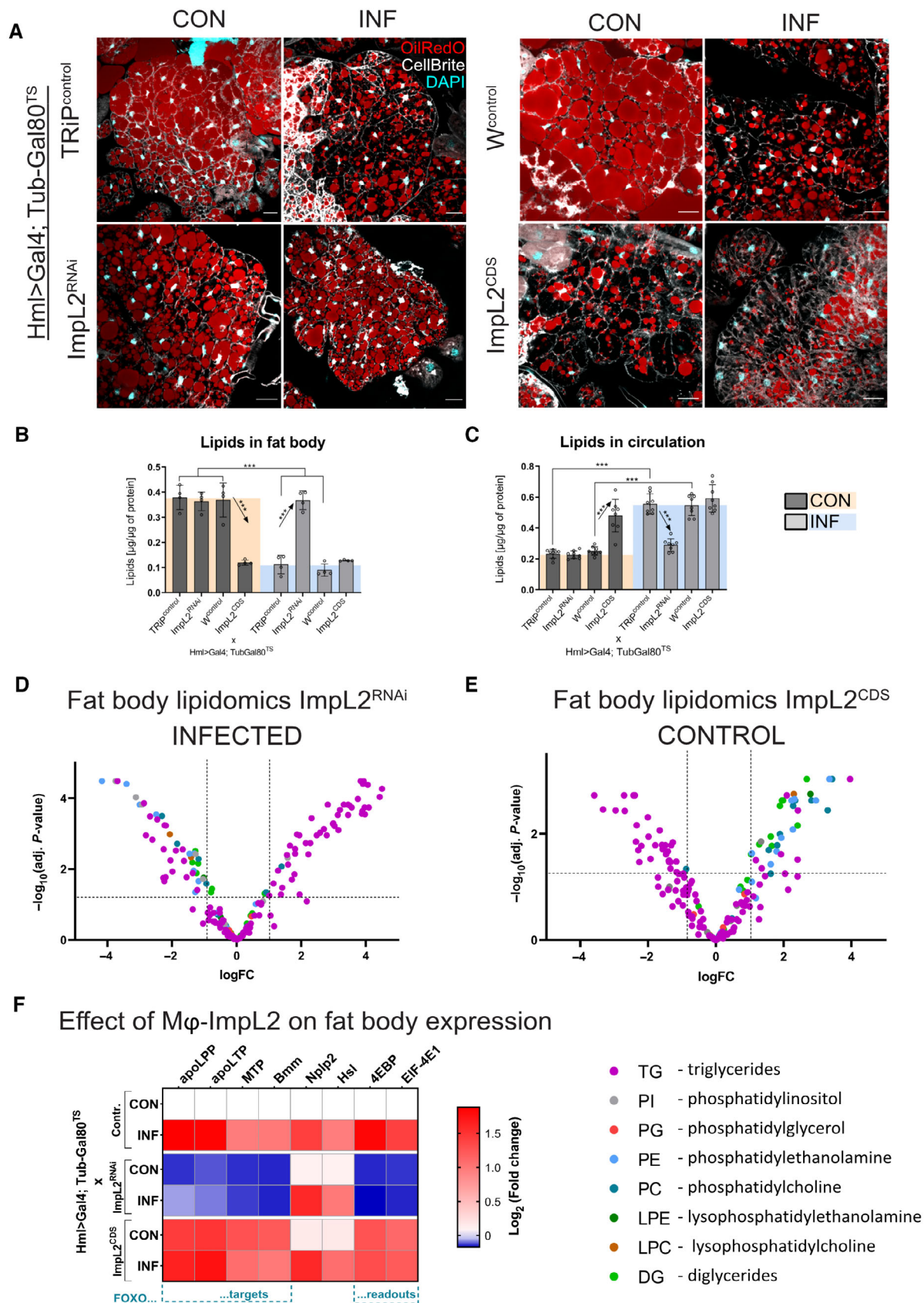
Figure 3.

Figure 3. Macrophage-derived IMPL2 directs the infection-induced mobilization of lipid stores.

A   Representative confocal microscopy images of the dissected fat body whole mounts of non-infected (CON) and infected (INF) flies with macrophage-specific *ImpL2* knockdown (*ImpL2^RNAi^*), overexpression (*ImpL2^CDS^*) and their respective controls (*TRiP^control^*, *w^control^*). The images illustrate the morphological changes of lipid droplets stained with OilRedO (red); nuclei are labeled by DAPI (cyan), CellBrite marks membranes (white). Scale bar represents 20 μm. Images of TRiP controls have been reused in Appendix Fig S15.

B, C   Lipid levels in the fat body (B) and circulation (C) of non-infected (CON) and infected (INF) flies with macrophage-specific *ImpL2* knockdown (*ImpL2^RNAi^*), overexpression (*ImpL2^CDS^*) and their respective controls (*TRiP^control^*, *W^control^*). *Results compared by 2way ANOVA Tukey's multiple comparisons test. The individual dots represent biological replicates with line/bar showing mean ± SD, asterisks mark statistically significant differences (***$P < 0.001$).*

D   Volcano plot showing the relative abundance of lipid classes in the fat body of infected flies with macrophage-specific *ImpL2* knockdown (*ImpL2^RNAi^*) compared to their infected controls (*TRiP^control^*). Data were obtained from six independent experiments.

E   Volcano plot showing the relative abundance of lipid classes in the fat body of non-infected (CON) flies with macrophage-specific *ImpL2* knockdown (*ImpL2^CDS^*) compared to their non-infected controls (*W^control^*). Data were obtained from six independent experiments.

F   Heat map showing the log$_2$-fold change in mRNA expression of genes of interest in the fat bodies dissected from non-infected (CON) and infected (INF) flies with macrophage-specific *ImpL2* knockdown (*ImpL2^RNAi^*), overexpression (*ImpL2^CDS^*) and their respective controls (*TRiP^control^*, *W^control^*). Differential expression is displayed as a log$_2$-fold change with respect to the gene expression level in control flies (average change for *TRiP^control^* and *W^control^*) under control conditions.

Data information: Expression levels normalized against rp49. All data presented in this figure were obtained 24 h post-infection. Data were obtained from four independent experiments if not stated otherwise. For analysis of metabolites; fat bodies from six individuals and hemolymph from 25 flies were used for each biological replicate. For lipidomic analysis, fat bodies from six individuals were used for each biological replicate. For qPCR analysis, fat bodies from six individuals were used for each biological replicate. 4EBP, Thor; apoLPP, apolipophorin; apoLTP, apolipoprotein lipid transfer particle; Bmm, brummer; EIF-4E1, eukaryotic translation initiation factor 4E1; Hsl, hormone sensitive lipase; MTP, microsomal triacylglycerol transfer protein; Nplp2, Neuropeptide-like precursor 2.

Source data are available online for this figure.

droplet morphology in adipocytes (Fig 4B–D). In conclusion, the effects of macrophage-derived IMPL2 on lipid metabolism in the fat body are mediated by the transcription factor FOXO, which is required for the mobilization of lipid stores upon infection.

Given that FOXO nuclear translocation is controlled by PI3K activity in situations of metabolic stress (Zhao *et al*, 2021), we analyzed the effect of Mφ-*ImpL2* manipulations on PI3K activity in the fat body. For this purpose, we employed a fly strain carrying *in vivo* PI3K reporter based on pleckstrin homology domain fused with GFP (tGPH; Britton *et al*, 2002). The signal, which is predominately localized to the plasma membrane in control flies, becomes more cytosolic in infected individuals, documenting decreased PI3K signaling in the fat body of infected flies. Since Mφ-*ImpL2^CDS^* phenocopies tGPH localization during infection even under control conditions (Fig 5A and B), we postulate that macrophage-derived *ImpL2* silences PI3K enzymatic activity in the fat body upon infection.

The impact of macrophage-derived *ImpL2* on FOXO and PI3K activity in the fat body indicates that the *ImpL2* effects may be mediated via silencing of insulin signaling since both these factors play a central role in insulin signaling in *Drosophila* (DiAngelo *et al*, 2009). This is consistent with the previously described function of *ImpL2* as an insulin signaling antagonist with a high affinity to circulating insulin and *Drosophila* insulin-like peptides (Honegger *et al*, 2008; Kwon *et al*, 2015).

Therefore, we aim to investigate the effects of insulin signaling on the redistribution of lipid stores upon infection. For this purpose, we generated flies with constitutively active (*FB > InR^CA^*) or genetically abrogated (*FB > InR^DN^* and *FB > PTEN^CDS^*) insulin signaling exclusively in the fat body by using a fat body-specific Gal4 driver (*FB-Gal4*; Grönke *et al*, 2003; see Fig EV2D for genotype explanations). While mere silencing of insulin signaling in the fat body of uninfected flies (*FB > InR^DN^* and *FB > PTEN^CDS^*) results in the depletion of lipid stores in this organ and their accumulation in the circulation, constitutive activation of insulin receptor (*FB > InR^CA^*) does not allow for the redistribution of lipids between these two compartments otherwise observed upon infection (Fig 5C and D and Appendix Fig S8A and B). In concordance with the previously observed morphology of

lipid droplets in the fat body, the flies bearing the *foxo* hypomorphic allele (*foxo^hypo.^*) were not able to induce mobilization of lipids from the fat body into the circulation upon infection as well as flies with *foxo* hypomorphic allele and macrophage-specific overexpression of *ImpL2* (*Hml > ImpL2^CDS^*; *foxo^hypo.^*; Fig 5C and D and Appendix Fig S8A and B). These data further support our conclusion that the metabolic effects of *ImpL2* are mediated by the activation of the FOXO transcriptional program.

Moreover, manipulation of insulin signaling in the fat body also affects the expression of genes involved in the assembly and mobilization of lipoproteins (*Apoltp*, *apolpp*, *Mtp*) in this tissue, which has been demonstrated above to respond to Mφ-*ImpL2* manipulations (Fig 5E and Appendix Fig S8C).

As anticipated, fat body-specific knockdown of genes involved in the assembly and mobilization of lipoproteins (*Apoltp*, *apolpp*, *Mtp*; see Appendix Fig S8D for RNAi efficiency and Fig EV2D for genotype descriptions) intervenes with the infection-induced depletion of lipid stores in the fat body and their mobilization into circulation (Fig 5F and G and Appendix Fig S9A and B).

Although the epistatic effect of macrophage-derived IMPL2 on insulin signaling in the fat body has not been explicitly demonstrated here, the data suggest that the effect of IMPL2 on the mobilization of lipid stores is likely mediated by attenuation of insulin signaling in the fat body, leading to increased production of lipoproteins into the circulation via a FOXO-induced transcriptional program (Fig 5H).

Redistribution of lipids toward activated macrophages is essential for resistance to bacterial infection

To address the question of whether *ImpL2*-induced lipoprotein mobilization is required for the redistribution of lipids toward infection-activated macrophages (Fig 1G and I), we assessed the incorporation of dietary ¹³C-FFAs and macrophage lipid content in flies with Mφ-*ImpL2* manipulations (see Appendix Fig S19 for experimental setup).

While infection in flies of control genotypes leads to the enhanced ¹³C-FFAs accumulation in activated macrophages at

A

B

C

Lipid droplet content
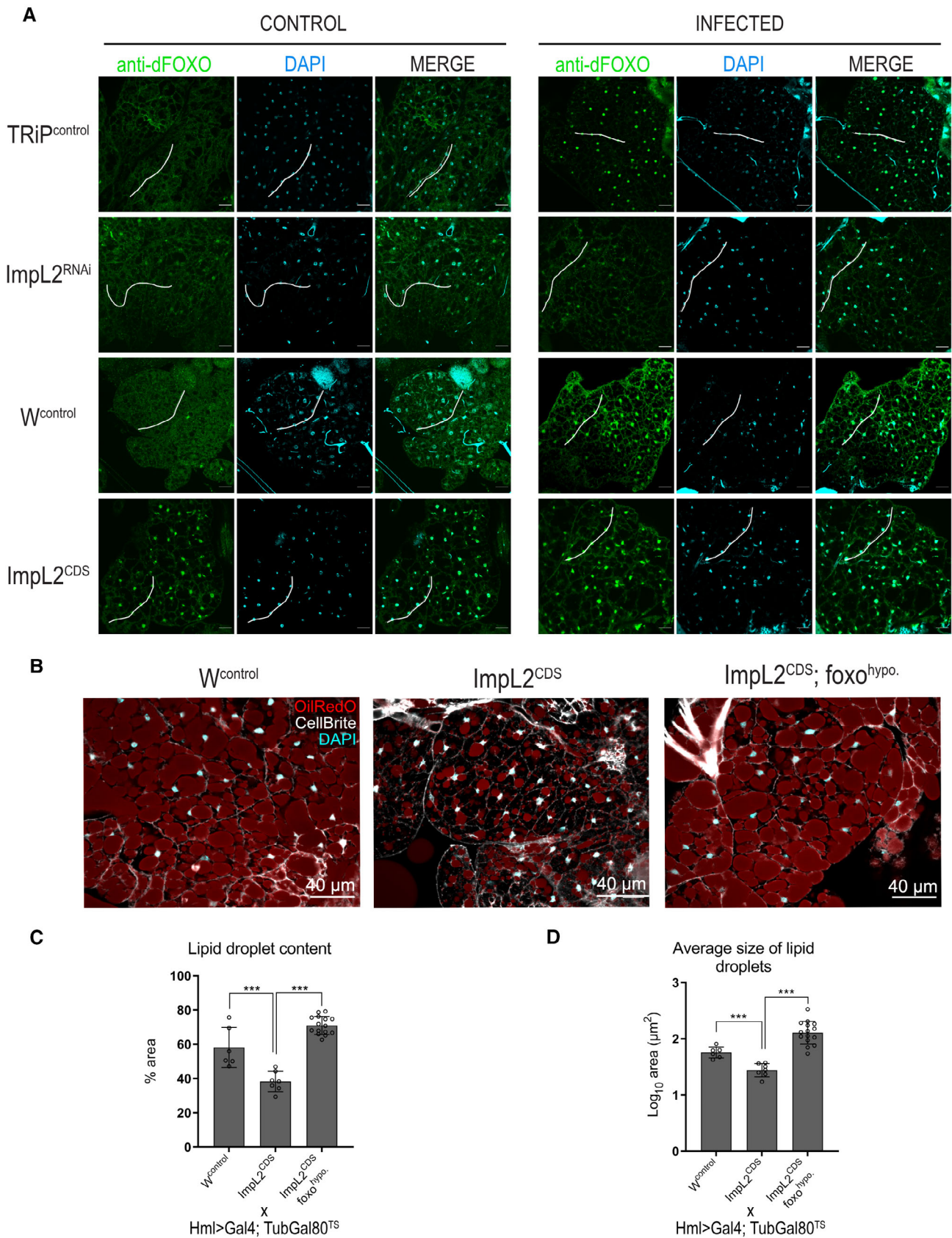
D

Average size of lipid droplets

Figure 4.

◀

Figure 4. Macrophage-derived IMPL2 affects FOXO signaling in the fat body.

A Representative confocal images showing subcellular localization of FOXO (stained by anti-dFOXO; green) in the fat body whole mounts dissected from non-infected (CON) and infected (INF) flies with macrophage-specific *ImpL2* knockdown (*ImpL2^RNAi^*), overexpression (*ImpL2^CDS^*) and their respective controls (*TRiP^control^* and *W^control^*). DAPI (cyan) marks nuclei. A white freehand line indicates the section for which the colocalization of DAPI and anti-dFOXO signals is displayed in intensity histograms in Fig EV5. Scale bar represents 20 μm.

B Representative confocal images showing the morphology of lipid droplets in the dissected fat body whole mounts dissected from noninfected control flies (*W^control^*), flies with macrophage-specific *ImpL2* overexpression (*ImpL2^CDS^*), and flies with macrophage-specific *ImpL2* overexpression in the hypomorphic *Foxo* mutant background (*ImpL2^CDS^*; *foxo^hypo.^*). Neutral lipids stained by OilRedO (red), CellBrite marks membranes (white), and DAPI nuclei (cyan).

C Percentage of the area occupied by lipid droplets in the fat body of non-infected control flies (*W^control^*), flies with macrophage-specific *ImpL2* overexpression (*ImpL2^CDS^*), and flies with macrophage-specific *ImpL2* overexpression in the hypomorphic *Foxo* mutant background (*ImpL2^CDS^*; *foxo^hypo.^*).

D The average size of lipid droplets in the fat body of non-infected control flies (*W^control^*), flies with macrophage-specific *ImpL2* overexpression (*ImpL2^CDS^*), and flies with macrophage-specific *ImpL2* overexpression in the hypomorphic *Foxo* mutant background (*ImpL2^CDS^*; *foxo^hypo.^*).

Data information: All data presented in this figure were obtained 24 h post-infection. In (C) and (D), data were obtained by analysis of dissected fat body whole mounts stained for neutral lipids (OilRedO). Images were captured by a confocal microscope. Data were obtained from six independent experiments. Results were compared by 2way ANOVA followed by Šídák's multiple comparisons test. The individual dots represent biological replicates with line/bar showing mean ± SD, asterisks mark statistically significant differences (***$P < 0.001$).

Source data are available online for this figure.

the expense of the fat body, this effect is diminished significantly in flies with Mφ-*ImpL2^RNAi^*. Contrary to that, mere Mφ-*ImpL2^CDS^* leads to enhanced ^{13}C-FFAs levels in macrophages in both infected and control flies (Fig 6A). Notably, we have not observed any marks of infection-induced anorexia as documented by comparable dietary uptake in flies regardless of treatment or their genotypes (Appendix Fig S10A).

That is consistent with elevated lipid content in macrophages of infected flies of control genotypes, which is not present in flies with Mφ-*ImpL2^RNAi^* but can be induced in uninfected flies by Mφ-*ImpL2^CDS^* (Fig 6B and Appendix Fig S10B). These data imply that macrophage-derived *ImpL2* is required for enhanced availability of lipids for the immune system and their accumulation in activated macrophages.

Further, we evaluated the importance of IMPL2-induced metabolic changes for immune function and resistance to infection. In this regard, we assessed the survival rate of flies with manipulated IMPL2 production in macrophages and flies with knockdown of genes required for the assembly and production of lipoproteins from the fat body.

Mφ-*ImpL2^RNAi^* leads to a significantly reduced phagocytic capacity of macrophages as documented by the decreased number of phagocytic events upon injection of a phagocytic marker (pHrodo-*S. aureus*; Fig 6C and D). In line with that, Mφ-*ImpL2^RNAi^* leads to increased pathogen load in these flies and decreased survival of infection, whereas flies with Mφ-*ImpL2^CDS^* display lower pathogen load and improved infection resistance (Fig 6E and F and Appendix Fig S10C). Cell-autonomous effects of Mφ-*Imp2* manipulations on the function of these cells were found to be insignificant since macrophages isolated from these flies show normal production of antimicrobial peptides, markers of metabolic polarization, and macrophage numbers (Appendix Figs S11–S15).

The importance of enhanced mobilization of lipoproteins during infection is documented by the decreased survival rate of flies with the fat body-specific knockdown of genes involved in lipoprotein assembly (*Apoltp*, *apolpp*, *Mtp*; Fig 7A and Appendix Fig S10D). Inhibition of mobilization of lipoproteins by fat body-specific knockdown of *apolpp* leads to decreased phagocytic capability of macrophages resulting in enhanced pathogen load in these flies at 24 hpi (Fig 7B–D). This is in concordance with enhanced lipoprotein

uptake by infection-activated macrophages compared to uninfected controls, as documented by the number of endocytic events of pHrodo-labeled low-density lipoproteins (LDL; Fig 7E and F), the enhanced proportion of macrophages containing lipid droplets in their cytosol as well as by accumulation of fluorescently-labeled FFAs (Appendix Figs S20 and S21). Increased uptake of lipids by activated macrophages and their subsequent processing is further supported by enhanced expression of genes involved in these processes (Appendix Figs S22 and S23).

Infection-activated mammalian liver macrophages release IGFBP7 to induce the mobilization of lipids from hepatocytes

The presented data demonstrate that the pro-inflammatory polarization of *Drosophila* macrophages is associated with the production of the signaling factor IMPL2 through the activity of the transcription factor HIF1α. IMPL2 subsequently triggers the mobilization of lipoproteins in the fat body to nutritionally supplement the immune system.

To investigate whether an analogous mechanism may be evolutionarily conserved and relevant in mammals, we focused on mammalian ImpL2 homolog *Insulin growth factor binding protein 7* (*Igfbp7*; Honegger *et al*, 2008). *Igfbp7* is a member of insulin growth factors with high affinity to human insulin and its functional and sequence homology to *ImpL2* has been described previously (Sloth Andersen *et al*, 2000; Roed *et al*, 2018).

First, we analyzed the production of IGFBP7 in human monocyte-derived macrophages (THP1 cells) during their bactericidal polarization. Pro-inflammatory polarization of THP1 cells induced by administration of *S. pneumoniae* or LPS leads to significant upregulation of IGFBP7 at both mRNA (Fig 8A) and protein levels (Fig 8B). Moreover, we revealed that IGFBP7 production in THP1 cells is controlled by the transcription factor HIF1α since the application of its inhibitor (KC7F2) or agonist (DMOG) has a major effect on IGFBP7 production in these cells regardless of their activation state (Fig 8A and B). Next, we investigated the effects of bacterial endotoxins (LPS) on IGFBP7 expression in liver macrophages (see Appendix Fig S24A for experimental design). Consistently with the data from THP1 cells, LPS induces IGFBP7 expression in liver macrophages isolated from mice and humans (Fig 8C and D).
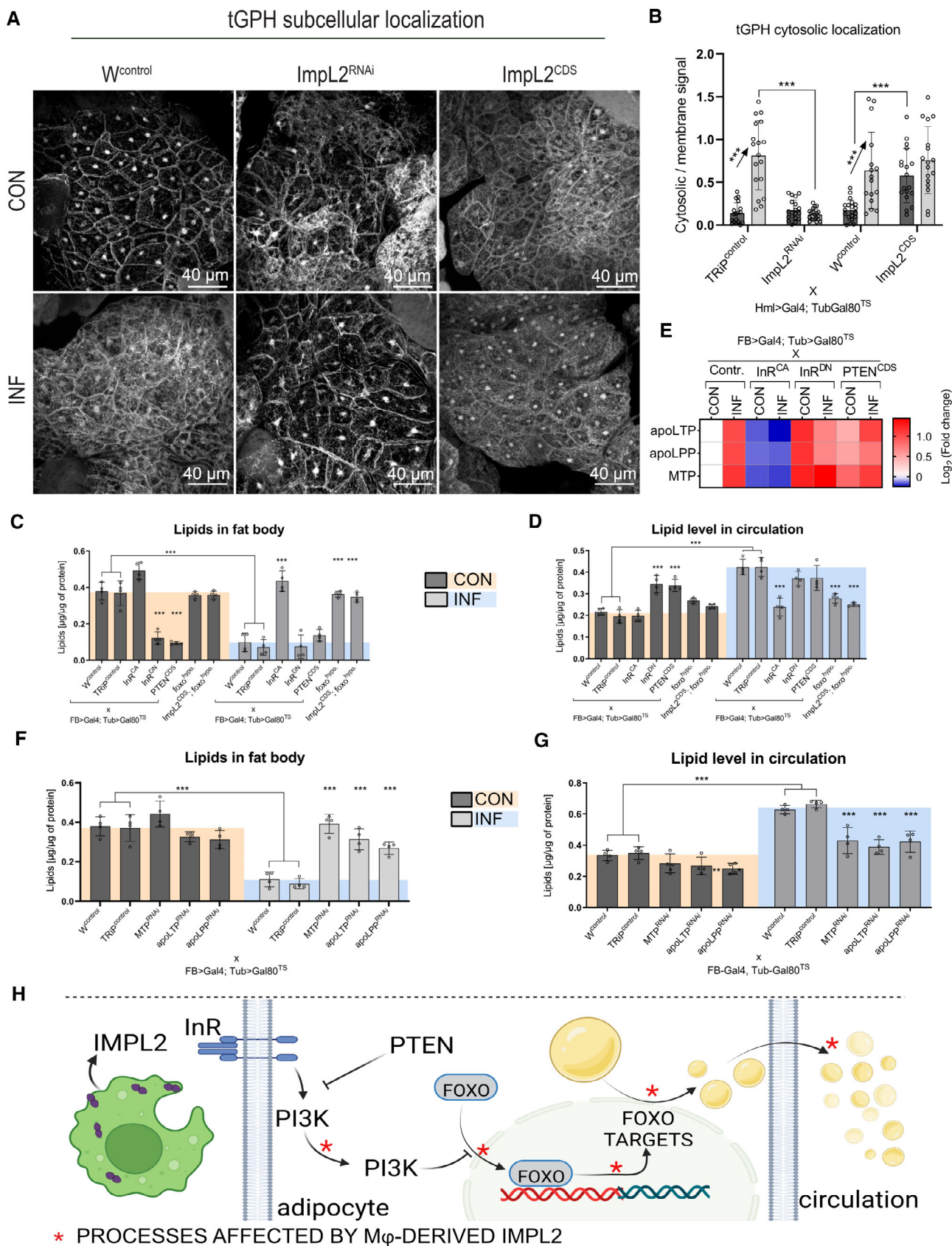
Figure 5.

◀

Figure 5. Macrophage-derived IMPL2 drives lipid mobilization in the fat body.

A Representative confocal images showing subcellular localization of the PI3K-activity reporter (tGPH; white) in the fat body whole mounts dissected from non-infected (CON) and infected (INF) control flies ($W^{control}$), flies with macrophage-specific *ImpL2* knockdown (*ImpL2^{RNAi}*) and overexpression (*ImpL2^{CDS}*). Images reconstructed from Z-stack consisting of a maximum projection of 10 layers.

B tGPH cytosolic localization in the fat body of non-infected (CON) and infected (INF) flies with macrophage-specific *ImpL2* knockdown (*ImpL2^{RNAi}*), overexpression (*ImpL2^{CDS}*) and their respective controls (*TRiP^{control}* and *W^{control}*) quantified as a proportion of the amount of signal in the membrane and cytosol regions. Individual dots in the plot represent biological replicates.

C, D The concentration of lipids in the fat body (C) and circulation (D) in non-infected (CON) and infected (INF) flies with fat body-specific overexpression of constitutively active or dominant negative form of insulin receptor (*InR^{CA}*, *InR^{DN}*), PTEN (*PTEN^{CDS}*), flies bearing *foxo* hypomorphic allele (*foxo$^{hypo.}$*), and in flies with a combination of *foxo* hypomorphic allele and macrophage-specific overexpression of ImpL2 (*Hml>ImpL2^{CDS}*; *foxo$^{hypo.}$*) compared to their respective controls (*W^{control}*; *TRiP^{control}*).

E Heat map showing the $\log_2$-fold change in mRNA expression of involved in mobilization of lipoproteins (*MTP*, *apoLTP*, *apoLPP*) in the fat body of noninfected (CON) and infected (INF) flies with fat body-specific overexpression of constitutively active or dominant negative form of insulin receptor (*InR^{CA}*, *InR^{DN}*), PTEN (*PTEN^{CDS}*), flies bearing *foxo* hypomorphic allele (*foxo$^{hypo.}$*), and in flies with a combination of *foxo* hypomorphic allele and macrophage-specific overexpression of ImpL2 (*Hml>ImpL2^{CDS}*; *TRiP^{control}*) compared to their respective controls (*W^{control}*; *TRiP^{control}*). Differential expression is displayed as a $\log_2$-fold change with respect to the gene expression level in control flies (average change for *TRiP^{control}* and *W^{control}*) under control experimental conditions. *Expression levels normalized against rp49.*

F, G The concentration of lipids in the fat body (F) and circulation (G) in non-infected (CON) and infected (INF) control flies (*W^{control}*; *TRiP^{control}*) and flies with fat body-specific knockdown of genes involved in the mobilization of lipoproteins (*MTP*, *apoLTP*, *apoLPP*).

H Schematic representation of the obtained results. Macrophage-derived IMPL2 silences insulin signaling in the fat body, resulting in decreased PI3K enzymatic activity, FOXO nuclear translocation, and enhanced mobilization of lipids from the fat body to the circulation.

Data information: All data presented in this figure were obtained 24 h post-infection. Data were obtained from four independent experiments if not stated otherwise. For analysis of metabolites; fat bodies from six individuals and hemolymph from 25 flies were used for each biological replicate. For qPCR analysis, fat bodies from six individuals were used for each biological replicate. In (C, D) and (F, G), the metabolite concentrations were normalized to the number of proteins in each sample. Results were compared by 2way ANOVA Tukey's multiple comparisons test. The individual dots represent biological replicates with line/bar showing mean ± SD, asterisks mark statistically significant differences (***P < 0.001). apoLPP, apolipophorin; apoLTP, Apolipoprotein lipid transfer particle; InR, insulin receptor; MTP, microsomal triacylglycerol transfer protein; PTEN, Phosphatase and tensin homolog.

Source data are available online for this figure.

To induce gene-specific knockdown exclusively in murine liver macrophages *in vivo*, we employed glucan particles as a macrophage-specific delivery tool that was developed for this purpose (Tencerova, 2020). Intravenously administered glucan particles loaded with siRNA against *Igfbp7* are specifically scavenged by liver macrophages and significantly reduce *Igfbp7* expression exclusively in these cells (Tencerova *et al*, 2015; Morgantini *et al*, 2019). Knockdown of *Igfbp7*, specifically in murine liver macrophages, results in decreased expression of apolipoprotein genes in hepatocytes *in vivo*, as revealed by their transcriptomic analysis (Fig 8F and Appendix Fig S24B).

To further test the IGFBP7 potential to induce lipoprotein production in human hepatocytes, we employed an organotypic 3D model of primary human liver cells in which cellular phenotypes closely resemble liver cells at the transcriptomic, proteomic, and metabolomic level *in vivo* (Bell *et al*, 2017; Vorrink *et al*, 2017; Oliva-Vilarnau *et al*, 2020). Indeed, the administration of human recombinant IGFBP7 on hepatocellular spheroids leads to elevated LDL and VLDL titers in culture media (Fig 8E).

Overall, our data indicate that *Igfbp7* may play an analogous role to *Drosophila ImpL2* since it is produced by liver macrophages in response to their pro-inflammatory polarization in a HIF1α-

Figure 6. Redistribution of lipids toward activated macrophages is essential for resistance to bacterial infection.

A Incorporation of dietary ^{13}C-labeled free fatty acids into the fat body, gut, and macrophages of non-infected (CON) and infected (INF) flies with macrophage-specific *ImpL2* knockdown (*Crq-Gal4>ImpL2^{RNAi}*), overexpression (*Crq-Gal4>ImpL2^{CDS}*) and their respective controls (*Crq-G4>UASGFP*). Data are expressed as relative incorporation of ^{13}C free fatty acids normalized to ^{12}C free fatty acids in the sample. Arrows indicate treatment- or genotype-induced changes compared to uninfected controls. *Guts from six flies, fat bodies from six individuals, and macrophages from 160 flies were used for each biological replicate.*

B The concentration of lipids in macrophages isolated from non-infected (CON) and infected (INF) flies with macrophage-specific *ImpL2* knockdown (*ImpL2^{RNAi}*), overexpression (*ImpL2^{CDS}*) and their respective controls (*TRiP^{control}*, *W^{control}*).

C The phagocytic capability of pHrodo-*S. aureus* in macrophages of infected flies with macrophage-specific *ImpL2* knockdown (*ImpL2^{RNAi}*), overexpression (*ImpL2^{CDS}*), and their respective controls (*TRiP^{control}*, *W^{control}*). The individual dots represent the $\log_{10}$-normalized numbers of the phagocytic events per cell. *Results were analyzed by Ordinary one-way ANOVA Dunnett's multiple comparisons test.*

D Representative confocal images of macrophages (*Crq>GFP*; green) of abdominal whole mounts dissected from infected flies with macrophage-specific *ImpL2* knockdown (*ImpL2^{RNAi}*), overexpression (*ImpL2^{CDS}*) and their respective controls (*TRiP^{control}*, *W^{control}*) injected with pHrodo-*S. aureus* (magenta).

E Pathogen load in flies with macrophage-specific knockdown of *ImpL2* (*ImpL2^{RNAi}*), overexpression (*ImpL2^{CDS}*), and their respective controls (*TRiP^{control}*, *W^{control}*) at 48 hpi. *Results were compared by Ordinary one-way ANOVA Dunnett's multiple comparisons test.*

F Survival of bacterial infection of flies with macrophage-specific knockdown of *ImpL2* (*ImpL2^{RNAi}*), overexpression (*ImpL2^{CDS}*), and their respective controls (*TRiP^{control}*, *W^{control}*). Survival curves for the respective uninfected genotypes are shown in dashed lines.

Data information: All data presented in this figure were obtained 24 h post-infection if not stated otherwise. In (B), (C), and (E), the individual dots represent biological replicates with line/bar showing mean ± SD. In (B), macrophages from 160 flies were used for each biological replicate; results were compared by 2way ANOVA Tukey's multiple comparisons test. In (F), three independent experiments were performed and combined into each survival curve; the number of individuals per replicate was at least 600 for each genotype; results were analyzed by Log-rank and Grehan-Breslow Wilcoxon tests. In (E), the individual dots in the plot represent the number of bacteria (colony forming units–CFUs) in thousands per fly. Asterisks mark statistically significant differences (***P < 0.001).

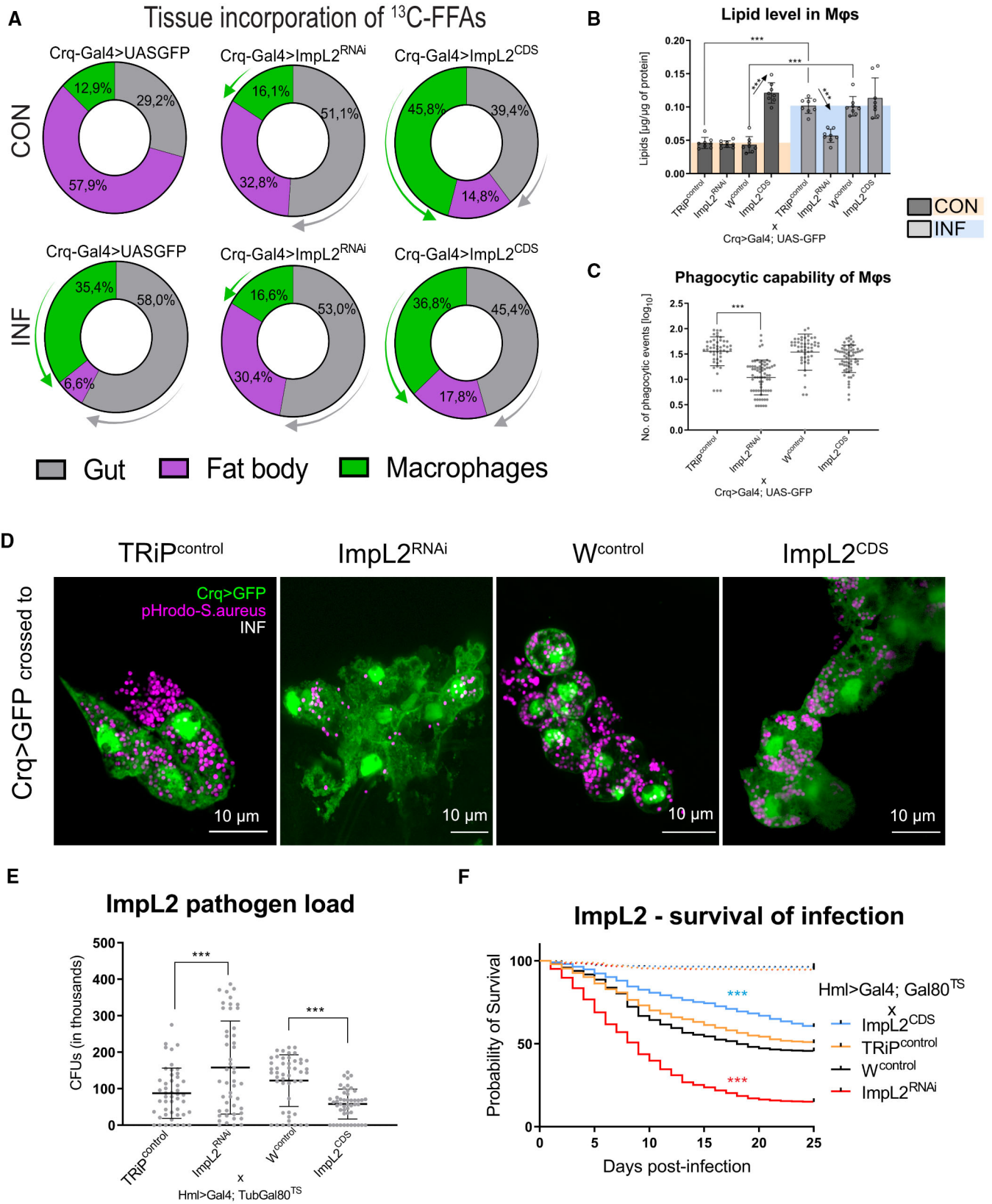Source data are available online for this figure.

Figure 6.

dependent manner and that IGFBP7 production by macrophages can elicit the production of lipoproteins from neighboring hepatocytes (Fig 8G).

Discussion

The pro-inflammatory polarization of macrophages is associated with extraordinary energy and nutritional demands that must be supplemented from external sources (Newsholme, 2021). To fight infection, an organism must significantly adjust systemic metabolism and relocate nutrients from stores toward the immune system (Ganeshan *et al*, 2019). In this regard, induction of insulin resistance has been proposed as a potentially adaptive mechanism for metabolic adaptation to infection (DiAngelo *et al*, 2009). However, the signal reflecting the nutritional demands of the activated immune system and the mechanism underlying the systemic metabolic changes remain largely unknown. In this work, we employed
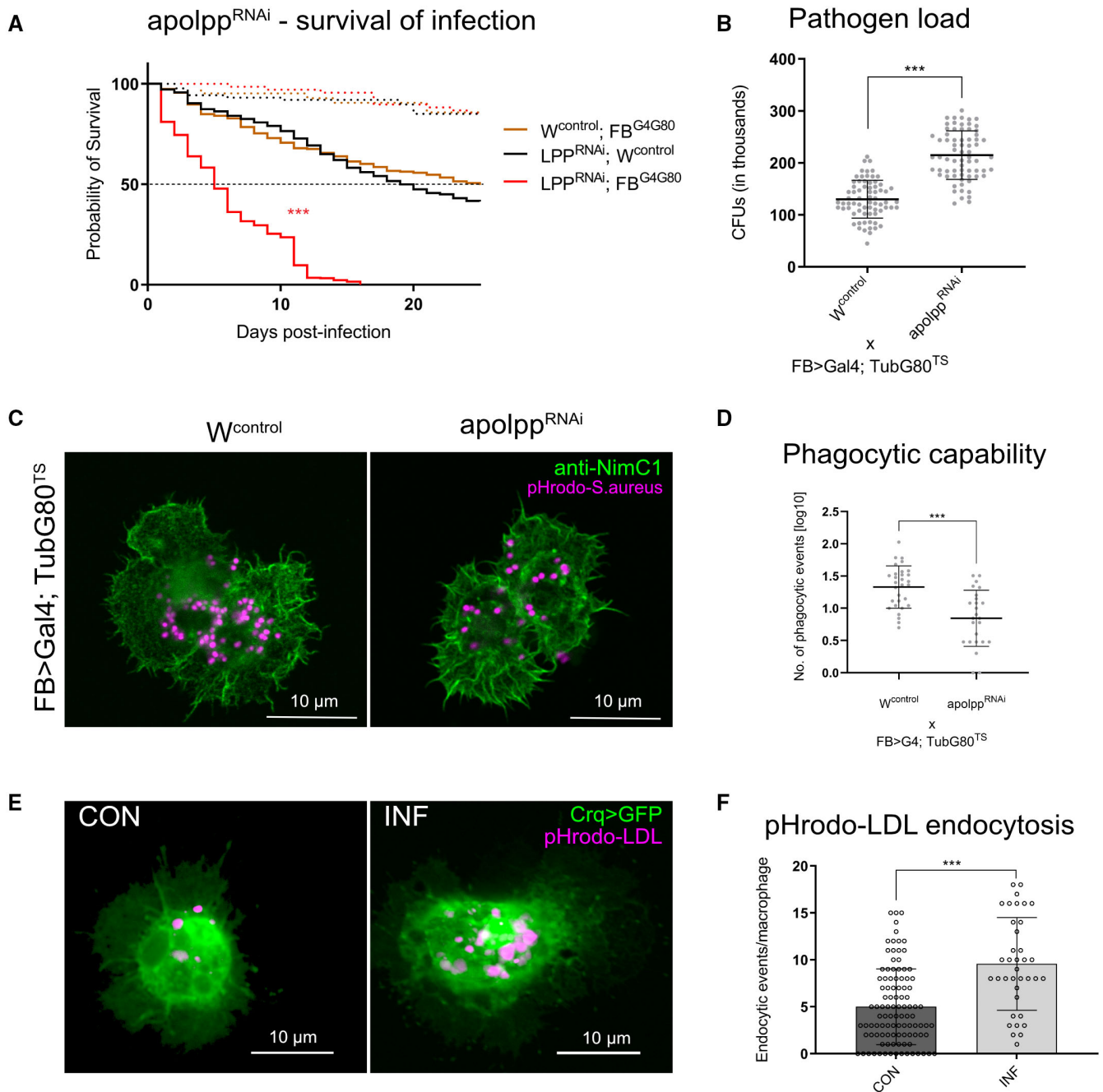

Figure 7.

Figure 7. Mobilization of lipoproteins from the fat body is required for efficient phagocytosis.

A   Survival of bacterial infection of flies with fat body-specific knockdown of *apolpp* (*LPP*^{RNAi}; *FB*^{G4G80}) and their respective controls (*W*^{control}; *FB*^{G4G80} and *LPP*^{RNAi}; *FB*^{G4G80}). Survival curves for the respective uninfected genotypes are shown in dashed lines.

B   Pathogen load in flies with fat body-specific knockdown of *apolpp* (apolpp^{RNAi}) and their respective controls (*W*^{control}) at 48 hpi. Results were compared by *Ordinary one-way ANOVA Dunnett's multiple comparisons test*.

C   Representative confocal images of macrophages (*Crq>GFP*; green) dissected from flies with fat body-specific knockdown of *apolpp* (apolpp^{RNAi}) and their respective controls (*W*^{control}) injected with pHrodo- *S. aureus* (magenta).

D   The phagocytic capability of pHrodo-*S. aureus* in macrophages of flies with fat body-specific knockdown of *apolpp* (apolpp^{RNAi}) and their respective controls (*W*^{control}). The individual dots represent the log$_{10}$-normalized numbers of the phagocytic events per cell. *Results were analyzed by Ordinary one-way ANOVA Dunnett's multiple comparisons test*.

E   Representative confocal images of macrophages (green) in non-infected (CON) and infected (INF) control flies (*Crq>GFP*; *TRiP*^{control}) injected with pHrodo-LDL depicting events of LDL endocytosis (magenta).

F   The number of endocytic events of low-density lipoproteins (LDL) per macrophage in non-infected (CON) and infected (INF) control flies (*Crq>GFP*; *TRiP*^{control}) injected with pHrodo-LDL. The individual dots mark the number of phagocytic events per cell. *Results were analyzed by Ordinary one-way ANOVA Dunnett's multiple comparisons test*.

Data information: Data were obtained from four independent experiments if not stated otherwise. In A, three independent experiments were performed and combined into each survival curve; the number of individuals per replicate was at least 600 for each genotype. Results were analyzed by Log-rank and Grehan-Breslow Wilcoxon tests. In (B), the individual dots in the plot represent the number of bacteria (colony forming units—CFUs) in thousands per fly; data were obtained from three independent experiments. Asterisks mark statistically significant differences (***$P < 0.001$) In (B), (D), and (F), individual dots in the plots represent biological replicates with line/bar showing mean ± SD. apolpp, apolipophorin.

Source data are available online for this figure.

a model of bacterial infection in *Drosophila* to reveal the mechanism connecting the metabolic remodeling of activated macrophages to a systemic metabolic switch.

In our previous work, we described that infection-activated *Drosophila* macrophages adopt aerobic glycolysis driven by the transcription factor HIF1α as a predominant metabolic pathway for energy production (Kedia-Mehta & Finlay, 2019; Krejčová *et al*, 2019). Here, we extend this observation and show that infection-activated macrophages exhibit increased lipid uptake and utilization in addition to aerobic glycolysis. Moreover, here we found that HIF1α activity leads to increased production of the signaling factor IMPL2 in these cells. Given that HIF1α is a crucial transcription factor governing the M1 metabolic shift (Corcoran & O'Neill, 2016), IMPL2 can be perceived as a signal translating the increased nutritional demands of activated macrophages to systemic metabolism.

It has been documented that IMPL2 is also secreted by genetically induced neoplastic tumors (Kwon *et al*, 2015), hypoxic muscles (Owusu-Ansah *et al*, 2013), and inflamed guts (Hang *et al*, 2014). Thus, IMPL2 production is not under all circumstances restricted exclusively to immune cells and may be coupled to strong metabolic activity and suddenly increased nutritional demands of virtually any tissue. Thus, the regulatory role of *ImpL2* may be crucial for the redistribution of resources during metabolic stress, and IMPL2 activity is not limited to pathological stress situations but may also have adaptive evolutionary significance.

Enhanced IMPL2 production has been shown to invoke systemic metabolic changes resembling cachexia-like wasting, leading to the depletion of lipid stores in the central metabolic organ (Figueroa-Clarevega & Bilder, 2015; Kwon *et al*, 2015). Bacterial infection and subsequent activation of immune-related cascades in the fat body leads to dramatic changes in its physiology and metabolism leading to mobilization of lipids as a part of the antibacterial immune response (Martínez *et al*, 2020; Zhao & Karpac, 2021). Consistent with this, we found that the production of IMPL2 by activated macrophages induces the mobilization of lipid stores from the fat body, leading to an elevated level of lipids in circulation and their subsequent accumulation in activated immune cells. The mechanism

underlying the effects of IMPL2 can be attributed to the alleviation of insulin signaling in the fat body, resulting in enhanced FOXO–induced mobilization of lipoproteins. This is consistent with the previous observation that IMPL2 exhibits a high affinity for circulating *Drosophila* insulin-like peptides, thus acting as a potent inhibitor of insulin signaling and coordinating larval growth and development (Honegger *et al*, 2008). Even though our data indicate that macrophage-derived IMPL2 induces mobilization of lipoproteins from the fat body, the participation of direct transport of dietary lipids toward activated immune cells cannot be excluded. Some of our data, however, do not support this eventuality. Analysis of lipid content in the gut indicates that infection leads to enhanced retention of lipids in this organ. Moreover, although genetic manipulation of *ImpL2* expression in macrophages affects the expression of *Apoltp* in the fat body, which is thought to be responsible for lipid transport from the gut, this manipulation does not affect gut lipid content significantly. We may thus speculate that in *Drosophila*, *Apoltp* may play a role in both lipid transport from the gut and mobilization of lipids from the fat body, as has been shown in other insect species (Arrese *et al*, 2001; Canavoso *et al*, 2004). Nevertheless, further investigation is needed in this regard.

Recently, it has been proposed that IMPL2 activity may cause the metabolic adaptations observed in the reproductive cast of ants that are required for the maturation of the ovaries, but the mechanism underlying this process has not been fully elucidated (Yan & Horng, 2020). Thus, our proposed mechanism of action of IMPL2 explains this phenomenon well.

We found that IMPL2 production interconnects the metabolic switch of activated macrophages to the mobilization of lipoproteins to supplement the metabolic needs associated with the bactericidal function of the immune system. Interventions of this mechanism at the level of IMPL2 production by macrophages, or lipoprotein mobilization from the fat body compromise the ability of macrophages to fight the bacterial pathogen, resulting in deterioration of the individual's resistance to infection. Thus, IMPL2-mediated metabolic changes are essential for an adequate immune response to extracellular bacteria. The presented data indicate that activated macrophages must be supplemented by lipids from external sources to

fight the pathogen efficiently. The increased uptake and accumulation of lipids by infection-activated macrophages may be attributed to their use for cell membrane remodeling, catecholamine synthesis, and epigenetic reprograming (Remmerie & Scott, 2018; Yan & Horng, 2020). Nonetheless, the link between increased lipid utilization and the bactericidal activity of *Drosophila* macrophages has not yet been satisfactorily elucidated.

Our data from mice and human experimental systems suggest that an analogous mechanism may be evolutionarily conserved. The *ImpL2* homolog *IGFBP7* is produced by liver macrophages upon their proinflammatory polarization and possesses the potential to induce the mobilization of LDL and VLDL from hepatocytes. Although the mechanism of IGFBP7 action on hepatocytes was not addressed in this study, we have previously shown that IGFBP7 binds directly to the insulin receptor in hepatocytes and induces systemic metabolic changes via regulation of ERK signaling in the liver (Roed *et al*, 2018). Our model is analogous to observations in obese mice and humans in which hepatic insulin resistance induces constitutive FOXO activation leading to increased lipoprotein production (Yan & Horng, 2020). Nonetheless, the effect of IGFBP7 and other
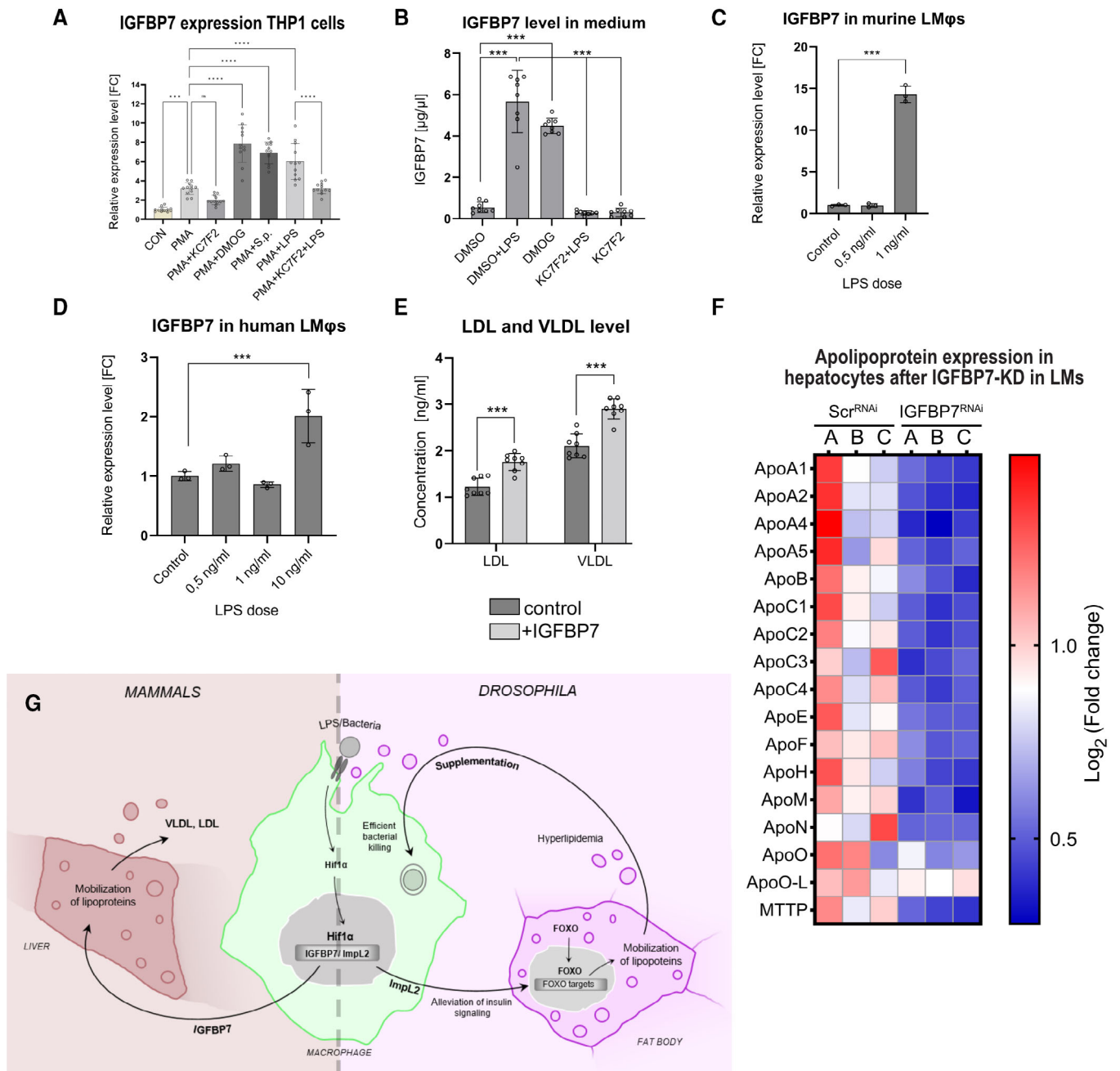

Figure 8.

Figure 8. Infection-activated liver macrophages release IGFBP7 to induce the mobilization of lipids from hepatocytes.

A   Expression of *IGFBP7* in the culture of THP-1 cells after administration of heat-killed streptococcus or LPS in combination with HIF1α inhibitor (KC7F2) or agonist (DMOG) and respective controls as measured by RT-qPCR. Expression levels normalized against ACTB are shown as a fold change relative to levels of IGFBP7 in non-activated THP1 cells (Mo) that were arbitrarily set to 1.

B   The concentration of IGFBP7 in culture media of THP-1 cells after administration of lipopolysaccharide (LPS) in combination with HIF1α inhibitor (KC7F2) or agonist (DMOG) and their respective control as measured by ELISA.

C   Expression of IGFBP7 in mouse liver macrophages in response to lipopolysaccharide treatment (LPS; 0.5 and 1 ng/ml) and their respective control. Expression levels are shown as a fold change relative to ACTB mRNA in buffer-treated controls that were arbitrarily set to 1.

D   Gene expression of IGFBP7 in human liver macrophages in response to lipopolysaccharide treatment (LPS; 0.5, 1, 10 ng/ml) and their respective control. Expression levels are shown as a fold change relative to ACTB mRNA in buffer-treated controls that were arbitrarily set to 1.

E   Concentration of low-density lipoproteins (LDL) and very-low-density lipoproteins (VLDL) in culture media obtained from the culture of human hepatocellular spheroids treated by human recombinant IGFBP7 protein (+IGFBP7) compared to buffer treated controls.

F   Heat map of transcriptomic data showing a $\log_2$-fold change in mRNA expression of apolipoproteins and lipoprotein synthetizing gene (Mttp) in hepatocytes isolated from mice with liver macrophage-specific knockdown of IGFBP7 (IGFBP7_KD) compared to scramble RNAi (Scr_RNAi) used as a control. Differential expression is displayed as a $\log_2$-fold change with respect to the average gene expression level in control replicates (Scr_RNAi).

G   Schematic representation of the proposed model. Foxo, forkhead box O; Hif1α, hypoxia-inducible factor 1 α; IGFBP7, Insulin growth factor binding protein 7; ImpL2, imaginal morphogenesis protein-late 2.

Data information: All data presented in this figure were obtained 24 h post-infection. Data were obtained from four independent experiments if not stated otherwise. In (A, B), the results were compared by 2way ANOVA Tukey's multiple comparisons test and by Ordinary one-way ANOVA Dunnett's multiple comparisons test in (C, D). The individual dots represent biological replicates with a line/bar showing mean ±. Samples from mice and humans, displayed in (C), (D) and (F), were isolated in three biological replicates. SD, asterisks mark statistically significant differences (*$P < 0.05$; ***$P < 0.001$; ****$P < 0.0001$). DMOG, dimethyloxallyl glycine; IGFBP7, insulin-like growth factor-binding protein 7; HIF-1α, hypoxia-inducible factor 1 α; KC7F2, N,N'-(disulfanediylbis(ethane-2,1-diyl))bis(2,5-dichlorobenzenesulfonamide).
Source data are available online for this figure.

cytokines on the mobilization of lipoproteins from the liver during bacterial infection requires further investigation.

Of particular note is the control of *ImpL2/IGFBP7* by the transcription factor HIF1α. In addition to the role of HIF1α in macrophage polarization during infection, increased activity of this transcription factor is a hallmark of progressive obesity and obesity-related diseases such as non-alcoholic fatty liver disease and atherosclerosis (Izquierdo *et al*, 2022). Therefore, the initially adaptive production of pro-inflammatory cytokines under HIF1α control may become maladaptive in the case of chronic macrophage polarization in adipose tissue and the liver.

In the context of the presented results, the cytokine-induced alleviation of insulin signaling in the liver may represent an initially adaptive mechanism by which macrophages secure nutrients for the function of the immune system during bacterial infection. However, chronic activation of this signaling in an infection-independent context may lead to the development of metabolic diseases.

Materials and Methods

Drosophila melanogaster strains and culture

The flies were raised on a diet containing cornmeal (80 g/l), sucrose (50 g/l), yeast (40 g/l), agar (10 g/l), and 10%-methylparaben (16.7 ml/l) and maintained in a humidity-controlled environment with a natural 12 h/12 h light/dark cycle at 25°C. Flies carrying Gal80 protein were raised at 18°C and transferred to 29°C 24 h before infection in order to degrade temperature-sensitive Gal80. Prior to the experiments, both experimental and control flies were kept in plastic vials on a sucrose-free cornmeal diet (cornmeal 53.5 g/l, yeast 28.2 g/l, agar 6.2 g/l and 10%-methylparaben 16.7 ml/l) for 7 days. Flies infected with *S. pneumoniae* were kept on a sucrose-free cornmeal diet in incubators at 29°C due to the temperature sensitivity of *S. pneumoniae*. Infected individuals were transferred to fresh vials every other day without the use of CO_2 to ensure good food conditions.

HmlG4G80: w^{1118}; HmlΔ-Gal4; P{tubPGal80ts}	Crossed by Tomas Dolezal	
w^{1118}; HmlΔ-Gal4 P{tubPGal80ts}/+; P{w[+mGT]=GT1}foxo^{BG01018}/UAS-ImpL2^{cds}	Crossed by Tomas Dolezal	
w^{1118}; HmlΔ-Gal4 P{tubPGal80ts}/+; tGPHGFP/TRiP^{control}	Crossed by Tomas Dolezal	
w^{1118}; PBac{sima-GFP.AC.FPTB}VK00037	Bloomington Drosophila Stock Center	BDSC: 42672
FbGal4/FbGal4; Tub-Gal80^{TS}/Tub-Gal80^{TS}	Provided by Katrin Kierdorf	
MTPRNAi	Bloomington Drosophila Stock Center	BDSC: 51872
ApoLPP^{RNAi}	Bloomington Drosophila Stock Center	BDSC: 28946
ApoLTP^{RNAi}	Bloomington Drosophila Stock Center	BDSC: 51937
yw; UAS-PTEN	Provided by Prof. Marek Jindra	
InR^{CA}	Bloomington Drosophila Stock Center	BDSC: 8263
InR^{DN}	Bloomington Drosophila Stock Center	BDSC: 8253
KKcontrol	Vienna Drosophila Resource Center	
ImpL2^{RNAi}	Bloomington Drosophila Stock Center	BDSC: 55855
ImpL2^{RNAi}	Bloomington Drosophila Stock Center	BDSC: 64936

ImpL2-RA-Gal4	Provided by Hugo Stocker	
ImpL2^{CDS}	Provided by Hugo Stocker	
20xUAS-6xmCherry	Bloomington Drosophila Stock Center	BDSC: 52267
CrqGal4>2xeGFP	Provided by Marc C. Dionne	
Hif1α[RNAi]: P{KK110834}VIE-260B	Vienna Drosophila Resource Center	VDRC: v106504
TRiP^{control}: y(1) v(1); P{y[+t7.7]=CaryP}attP2	Bloomington Drosophila Stock Center	BDSC: 36303
w: w^{1118}	Genetic background based on CantonS	

Bacterial strain and fly injection

The *Streptococcus pneumoniae* strain EJ1 was stored at −80°C in Tryptic Soy Broth (TSB) media containing 10% glycerol. For the experiments, bacteria were streaked onto agar plates containing 3% TSB and 100 mg/ml streptomycin and subsequently incubated at 37°C in 5% CO_2 overnight. Single colonies were inoculated into 3 ml of TSB liquid media with 100 mg/ml of streptomycin and 100,000 units of catalase and incubated at 37°C + 5% CO_2 overnight. Bacterial density was measured after an additional 4 h so that it reached an approximate 0.4 OD600. Final bacterial cultures were centrifuged and dissolved in PBS so the final OD reached 2.4. The *S. pneumoniae* culture was kept on ice before injection and during the injection itself. Seven-day-old males were anesthetized with CO_2 and injected with a 50 nl culture containing 20,000 *S. pneumoniae* bacteria or 50 nl of mock buffer (PBS) into the ventrolateral side of the abdomen using an Eppendorf Femtojet microinjector.

Survival analysis

Streptococcus-injected flies were kept at 29°C in vials with approximately 30 individuals per vial and were transferred to fresh food every other day. Dead flies were counted daily. At least three independent experiments were performed and combined into a single survival curve generated in GraphPad Prism software; individual experiments showed comparable results. The average number of individuals was more than 500 for each genotype and replicate.

Pathogen load measurement

Single flies were homogenized in PBS using a motorized plastic pestle in 1.5 ml tubes. Bacteria were plated in spots onto TSB (*S. pneumoniae*) agar plates containing streptomycin in serial dilutions and incubated overnight at 37°C before manual counting. Pathogen loads of 16 flies were determined for each genotype and treatment in each experiment; at least three independent infection experiments were conducted and the results were combined into one graph (in all presented cases, individual experiments showed comparable results).

Isolation of macrophages

GFP-labeled macrophages were isolated from *Crq > Gal4 UAS-eGFP* male flies using fluorescence-activated cell sorting (FACS; Krejčová *et al*, 2019). Approximately 200 flies were anesthetized with CO_2, washed in PBS, and homogenized in 600 ml of PBS using a pestle. The homogenate was sieved through a nylon cell strainer (40 μm).

This strainer was then additionally washed with 200 μl of PBS, which was added to the homogenate subsequently. The samples were centrifuged (3 min, 4°C, 3,500 rpm) and the supernatant was washed with ice-cold PBS after each centrifugation (three times). Before sorting, samples were transferred to FACS polystyrene tubes using a disposable bacterial filter (50 μm, Sysmex) and macrophages were sorted into 100 μl of PBS using an S3™ Cell Sorter (BioRad). Isolated cells were verified by fluorescence microscopy and differential interference contrast. Different numbers of isolated macrophages were used in different subsequent analyses. To this end, different numbers of flies were used for their isolation, specifically 90 flies were used to isolate 20,000 macrophages for qPCR analysis; approximately 160 flies were used to isolate 50,000 macrophages for metabolic analysis; approximately 300 flies were used to isolate 100,000 and 200,000 macrophages for lipidomic and transcriptomic analyses.

Gene expression analysis

Gene expression analyses were performed on several types of samples: six whole flies, six thoraxes, six fat bodies, or 20,000 isolated macrophages. For a description of the dissection procedure see Appendix Fig S25. Macrophages were isolated by a cell sorter (S3e Cell Sorter, BioRad) as described previously (Krejčová *et al*, 2019) while dissections were made in PBS, transferred to TRIzol Reagent (Invitrogen), and homogenized using a DEPC-treated pestle. Subsequently, RNA was extracted by TRIzol Reagent (Invitrogen) according to the manufacturer's protocol. Superscript III Reverse Transcriptase (Invitrogen) primed by oligo(dT)20 primer was used for reverse transcription. Relative expression rates for particular genes were quantified on a 384CFX 1000 Touch Real-Time Cycler (BioRad) using the TP 2x SYBR Master Mix (Top-Bio) in three technical replicates with the following protocol: initial denaturation—3 min at 95°C, amplification—15 s at 94°C, 20 s at 56°C, 25 s at 72°C for 40 cycles. Melting curve analysis was performed at 65–85°C/step 0.5°C. The primer sequences are listed in the Key Resources Table. The qPCR data were analyzed using double delta Ct analysis, and the expressions or specific genes were normalized to the expression of Ribosomal protein 49 (Rp49) in the corresponding sample. The relative values (fold change) to control are shown in the graphs.

Metabolite measurement

To measure metabolite concentration, isolated macrophages, whole flies, fat bodies, or hemolymph (circulation) were used. Hemolymph was isolated from 25 adult males by centrifugation (14,000 rpm,

5 min) through a silica-gel filter into 50 μl of PBS. For measurement of metabolites from whole flies, five flies were homogenized in 200 μl of PBS and centrifuged (3 min, 4°C, 8,000 rpm) to discard insoluble debris. 50,000 macrophages were isolated by cell sorter (S3e Cell Sorter, BioRad) as described in the section Isolation of macrophages. For analysis of fat body metabolites, the fat body from six flies was dissected and homogenized in ice-cold PBS. Fraction of fat body was used for quantification of carbohydrates and part was used for isolation of lipid fraction by adapted Bligh and Dyer method for assaying of cholesterol, cholesteryl-ester, and triglycerides. The concentration of metabolites was normalized per protein in the sample. Half of all samples were used for the quantification of proteins. Samples for glucose, glycogen, trehalose, and glyceride measurement were denatured at 75°C for 10 min, whereas samples for protein quantification were frozen immediately at −80°C. Glucose was measured using a Glucose (GO) Assay (GAGO-20) Kit (Sigma) according to the manufacturer's protocol. The colorimetric reaction was measured at 540 nm. For glycogen quantification, a sample was mixed with amyloglucosidase (Sigma) and incubated at 37°C for 30 min. A Bicinchoninic Acid Assay (BCA) Kit (Sigma) was used for protein quantification according to the supplier's protocol and the absorbance was measured at 595 nm. Cholesterol and cholesteryl esters were measured on isolated lipid fractions by using Cholesterol/Cholesteryl Ester Quantitation Kit (Sigma) according to the supplier's protocol. Glycerides were measured using a Triglyceride quantification Colorimetric/Fluorometric Kit (Sigma). For trehalose quantification, a sample was mixed with trehalase (Sigma) and incubated at 37°C for 30 min. Samples for metabolite concentration were collected from three independent experiments.

Staining of lipid droplets

Flies were dissected in Grace's Insect Medium (Sigma) and subsequently stained with DAPI and Cell Brite Fix Membrane Stain 488 (Biotium) diluted with Grace's Insect Medium according to the manufacturer's protocol at 37°C. Tissues were washed in PBS and then fixed with 4% PFA (Polysciences). After 20 min, the tissues were washed in PBS and pre-washed with 60% isopropanol. Dissected abdomens were then stained with OilRedO dissolved in 60% isopropanol for 10 min. The tissues were then washed with 60% isopropanol and mounted in an Aqua Polymount (Polysciences). Tissues were imaged using an Olympus FluoView 3000 confocal microscope (Olympus). The content of lipids in adipose tissue and the size of lipid droplets were analyzed using Fiji software. Flies for the analysis of lipid droplets in the fat body were collected from three independent experiments and representative images are shown.

Lipidomic analysis

Fat bodies from six flies and one hundred thousand isolated macrophages were obtained for each analyzed group. Tissue lipid fraction was extracted by 500 μl of cold chloroform: methanol solution (v/v; 2:1). The samples were then homogenized by a Tissue Lyser II (Qiagen, Prague, Czech Republic) at 50 Hz, −18°C for 5 min and kept further in an ultrasonic bath (0°C, 5 min). Further, the mixture was centrifuged at 10,000 rpm at 4°C for 10 min followed by the removal of the supernatant. The extraction step was repeated under the same conditions. The lower layer of pooled supernatant was

evaporated to dryness under a gentle stream of Argon. The dry total lipid extract was re-dissolved in 50 μl of chloroform: methanol solution (v/v; 2:1) and directly measured using previously described methods (Bayley *et al*, 2020). Briefly, high-performance liquid chromatography (Accela 600 pump, Accela AS autosampler) combined with mass spectrometry LTQ-XL (all Thermo Fisher Scientific, San Jose, CA, USA) were used. The chromatographic conditions were as follows: Injection volume 5 μl; column.

Gemini 3 μM C18 HPLC column (150 × 2 mm ID, Phenomenex, Torrance, CA, USA) at 35°C; the mobile phase (A) 5 mM ammonium acetate in methanol with ammonia (0.025%), (B) water and (C) isopropanol: MeOH (8:2); gradient change of A:B:C as follows: 0 min: 92:8:0, 7 min: 97:3:0, 12 min: 100:0:0, 19 min: 93:0:7, 20–29 min: 90:0:10, 40–45 min: 40:0:60, 48 min: 100:0:0, and 50–65 min: 92:8:0 with flow rate 200 μl/min. The mass spectrometry condition: positive (3 kV) and negative (−2.5 kV) ion detection mode; capillary temperature 200°C. Eluted ions were detected with full scan mode from 200 to 1,000 Da with the collisionally induced MS2 fragmentation (NCE 35). Data were acquired and processed by means of XCalibur 4.0 software (Thermo Fisher). The corrected areas under individual analytical peaks were expressed in percentages assuming that the total area of all detected is 100%. Lipidomics data were subsequently analyzed in the online platform LipidSuite (https://suite.lipidr.org/; Mohamed & Hill, 2021). Data were inputted by the K-Neares Neighbors method (KNN), and normalization was performed by the PQN algorithm. Subsequently, data were explored by PCA and OPLS-DA methods. Differential analysis of lipidomic data was done by univariate analysis and visualized in Volcano plots.

Immunostaining

Flies were dissected in ice-cold PBS and fixed with 4% PFA in PBS (Polysciences) for 20 min. After three washes in PBS-Tween (0.1%), nonspecific binding was blocked by 10% NGS in PBS for 1 h at RT. Tissues were then incubated with primary antibodies (for NimC1: Mouse anti-NimC1 antibody P1a + b, 1:100, kindly provided by István Andó (Kurucz *et al*, 2007); for Foxo: Rabbit anti-Foxo, CosmoBio, 1:1,000; for tGPH: Rabbit anti-GFP, ABfinity, 1:100) at 4°C overnight. After washing the unbound primary antibody (three times for 10 min in PBS-Tween), the secondary antibody was applied at a dilution of 1:250 for 2 h at RT (Goat anti-Mouse IgG (H + L) Alexa 555, Invitrogen or Goat anti-Rabbit IgG (H + L) Cy2, Jackson-Immunoresearch). Nuclei were stained with DAPI. Tissues were mounted with Aqua Polymount (Polysciences). Tissues were imaged using an Olympus FluoView 3000 confocal microscope (Olympus) and images were reconstructed using Fiji software. Foxo localization was detected by Plot-Profile analysis using Fiji software. For tGPH activity, confocal images were analyzed by using a plot profile (FIJI) under an arbitrarily defined line connecting two nuclei of neighboring cells and crossing the membrane in the middle. The ratio between cytosolic and membrane signals is displayed in the plot.

Incorporation of ^{13}C free fatty acids

For assaying 13C-FFA distribution post-infection, males were fed standard fly food covered on its surface with 50 μl [13]C Fatty Acid

Mix (Cambridge Isotope Laboratories), 5 mg/ml in chloroform per each vial for 5 h. After 5 h FFAs can be detected in the gut, but are not incorporated into other body compartments (as documented by Bodipy-labeled FFAs). Thereafter, the flies were split into control and experimental groups and injected with buffer or *S. pneumoniae*, and transferred to a fresh vial containing unlabeled food. After 24 h, six guts and six fat bodies were dissected in PBS and 50,000 macrophages were isolated by cell sorter from 160 individuals. Lipid fraction from the samples was isolated through the standard Bligh and Dyer procedure and free fatty acids were deliberated from complexes by a lipase from *Aspergillus niger*. Homogenized and filtered chloroform extracts (100 μl) were put in glass inserts in 2 ml chromatographic vials and their 13C enrichment was analyzed compound-specific. 1 μl was injected in a split/splitless injector of a gas chromatograph, GC (Trace 1310, Thermo, Bremen, Germany), injector at 250°C. The injection was splitless for 1.5 min, then split with flow 100 ml/min for the next 1 min, and 5 ml/min (gas saver) for the rest of the analysis. Semipolar capillary column Zebron, ZB-FFAP (Phenomenex, Torrance CA, USA, 30 m × 0.25 mm × 0.25 μm film thickness) with a flow rate of 1.5 ml/min of helium was used as a carrier. The temperature program was: 50°C during injection and for the next 2 min, then 50–200°C with a slope of 30°C/min, 200–235°C with a slope of 3°C/min, and hold at 235°C for the rest 32 min (total run time ca 51 min). Eluting compounds were oxidized to CO_2 via IsoLink II interphase (Thermo, Bremen, Germany) at 1000°C and introduced to continuous-flow isotope ratio MS (Delta V Advantage, Thermo, Bremen, Germany). Compounds were identified using retention times of fatty acid standards. 13C sample abundance was expressed in At-% 13C and "13C excess" calculated as follow:

$$13C\ excess = A13Cs - A13Cn$$

where A13Cs is the absolute 13C abundance of labeled samples and A13Cn absolute 13C abundance of natural lipids.

Transcriptomic analysis

For transcriptomic analysis, macrophages from flies infected by *S. pneumoniae* or injected with PBS were isolated by cell sorter as described in the section "Isolation of macrophages". Two hundred thousand macrophages were used for the isolation of RNA by TRIzol (Ambion). Sequenation libraries were prepared by using siTOOLs riboPOOL *D. melanogaster* RNA kit (EastPort) followed by subtraction of ribosomal fraction by NEBNext Ultra II Directional RNA kit (Illumina). The quality of prepared RNA libraries was assayed by Bioanalyzer and all samples reached an RIN score over the threshold of 7. Sequencing analysis was performed by using the NovaSeq instrument (Illumina). Raw sequencing data were processed by standard bioinformatics workflow for trimming barcodes and adapters. Trimmed reads were aligned to reference *D. melanogaster* genome BDGP6.95 (Ensembl release). Trimming, mapping, and analysis of quality were performed in CLC Genomic Workbench 21.0.5 software via standard workflow for RNA-seq and Differential gene expression analysis. A subsequent search of transcriptomic data for enhanced and silenced pathways and biological processes was done by using TCC (Sun *et al*, 2013), and iDep94 (Ge *et al*, 2018) platforms combined with String and FlyMine databases.

Chip-qPCR assay

The Pro-A Drosophila CHIP Seq Kit (Chromatrap) was used to co-immuno-precipitate genomic regions specifically bound by the transcription factor HIF1α. A transgenic fly strain carrying the Hif1α protein fused to GFP (BDSC: 42672) was used for this purpose. The procedure was performed according to the supplier's instructions. Briefly, the slurry was prepared by homogenizing 10 infected or PBS-injected males in three biological replicates. The Rabbit Anti-GFP antibody (ABfinity) was bound to the chromatographic column. Genomic DNA was fragmented to an approximate size of 500 bp by three cycles of 60-s sonication. The fragment size was verified by gel electrophoresis. All samples were tested with positive and negative controls. The amount of precipitated genomic fragments was normalized to the number of fragments in the slurry before precipitation. The ImpL2-RA promoter sequence was covered with seven primer pairs corresponding to the 500-bp bins upstream of the transcription start site previously assessed in the *in silico* analysis. The genomic region of S-adenosylmethionine synthetase was used as a negative control since it does not contain any sequences of hypoxia response elements. Primer sequences are listed in the Key Resources Table. The amount of HIF1α-bound regions of the ImpL2 promoter was quantified on a 96CFX 1000 Touch Real-Time Cycler (BioRad) using TP 2× SYBR Master Mix (Top-Bio) in three technical replicates with the following protocol: initial denaturation—3 min at 95°C, amplification—15 s at 94°C, 20 s at 56°C, 25 s at 72°C for 40 cycles. Melting curve analysis was performed at 65–85°C/step 0.5°C. The qPCR data were analyzed using double delta Ct analysis.

Phagocytic activity

To analyze the phagocytic rate, flies were infected with 20,000 *S. pneumoniae* and after 24 h, they were injected with 50 nl of pHrodo™ Red *S. aureus* (Thermo Fischer Scientific). After 1 h, the abdomens of flies were dissected in PBS and then fixed for 20 min with 4% PFA. Aqua Polymount (Polysciences) was used to mount the sample. Macrophages were imaged using an Olympus FluoView 3000 confocal microscope and red dots depicting phagocytic events were manually counted per cell.

Lipoprotein uptake

To analyze lipoprotein uptake by *Drosophila* macrophages, Buff injected or infected Crq > GFP flies were injected at 24 hpi with pHrodo™ Red LDL (Invitrogen) into the ventrolateral side of the abdomen using an Eppendorf Femtojet microinjector. After 1 h, the fly abdomens were opened in PBS and subsequently fixed for 20 min with 4% PFA in PBS (Polysciences). Aqua Polymount (Polysciences) was used to mount the sample. Macrophages were imaged using an Olympus FluoView 3000 confocal microscope. LDL pHrodo signal was counted manually from 10 flies for each group.

THP-1 cell lines

THP-1 cells were cultured at 37°C, 5% CO_2, in RPMI-1640 medium (Sigma), supplemented with 2 mM glutamine (Applichem), 2 g/l sodium bicarbonate (J&K Scientific), 10% FBS (Biosera) and 100 mg/l streptomycin (Sigma). Prior to the experiment, cells were

transferred to 24-well plates at 10^5 cells/well in four biological replicates. THP-1 cells were activated with phorbol-12-myristate-13-acetate (200 ng/ml, MedChemExpress). After 24 h, *S. pneumoniae* bacteria were added (MOI 50 bacteria/macrophage) or LPS (100 ng/ml; and the plate was centrifuged briefly (2 min, 200 *g*). Following 6-h incubation, the cells were washed with RPMI-1640 medium, and fresh RPMI-1640 supplemented with gentamycin (0.1 mg/ml, Sigma) was added. After 1 h incubation, the medium was replaced with RPMI-1640 supplemented with penicillin–streptomycin (1%, Biosera). After another 17 h, the cells were harvested into TRIzol Reagent (Invitrogen) followed by RNA isolation. In experiments with Hif1α agonist (DMOG—50 mg/ml) and antagonist (KC7F2—25 mg/ml), the Hif1a-affecting drugs were administered 24 h before exposure of cells to LPS. DMSO was used instead of drug treatments in controls. For quantification of IGFBP7 concentration, the media were harvested and diluted 1:10. IGFBP7 protein level was quantified according to the manufacturer's protocol (Human IGFBP7/Igfbp Rp1 ELISA Kit PicoKine, BosterBio).

Expression analysis of IGFBP7 in mice and human LMs and transcriptomic analysis of hepatocytes

Isolation of RNA, real-time qPCR and RNA library preparation

RNA extraction and purification were performed by using TRIzol reagent according to the manufacturer's instructions (Thermo Fisher Scientific, 15596018). For real-time qPCR, cDNA was synthesized from 0.5 μg of total RNA with the iScript cDNA Synthesis kit (Bio-Rad) according to the manufacturer's instructions. Synthesized cDNA along with forward and reverse primers and Advanced Universal SYBR Green Supermix was run on a CFX96 Real-Time PCR System (Bio-Rad). β-actin (Actb) was used as a reference gene in mice and humans. RNA integrity was determined with an Agilent Bioanalyzer. Libraries from mouse RNA were prepared with the TruSeq Stranded mRNA kit (Illumina) and libraries from human RNA were prepared with the SMARTer Ultra-Low RNA kit (Clontech). The concentration of the indexed libraries was determined by real-time qPCR using the Universal Kapa Library Quantification kit (KAPA Biosystems). Final libraries were normalized and sequenced on an Illumina HiSeq 2000 sequencer.

Isolation of liver macrophages and hepatocytes from mice

Liver macrophages and hepatocytes were isolated as previously described. Briefly, the livers of anesthetized mice were first perfused with calcium-free Hank's balanced salt solution (HBSS), followed by collagenase digestion. After digestion, hepatocytes were released by mechanical dissociation of the lobes and underwent several steps of filtration with calcium-containing HBSS and centrifugation at 50 *g* for 3 min. The resulting hepatocyte pellet was washed twice and plated. The supernatant containing non-parenchymal cells was loaded onto a Percoll gradient (25 and 50%) and centrifuged at 2,300 rpm for 30 min at 4°C. The interphase ring with enriched liver macrophages was collected. Cells were then plated for 30 min and washed twice before RNA or protein was extracted for subsequent analyses.

Isolation of liver macrophages from humans

Freshly obtained liver biopsies were cut into small pieces and immediately digested in RPMI medium containing collagenase II

(0.25 mg/ml; Sigma, C6885) and DNase I (0.2 mg/ml; Roche, 1010415900) at 37°C for 30 min. Single-cell suspensions were filtered through a cell strainer (75 μm) and centrifuged at 50 *g* for 3 min. The supernatant containing non-parenchymal cells was loaded onto a Percoll gradient and liver macrophages were isolated as described above. For details concerning this experiment view part Methods and Supplementary Methods in (Tencerova, 2020).

GeRP administration by intravenous injection *in vivo*

Glucan shells (GS) were prepared by using a previously published protocol (Tesz *et al*, 2011). Briefly, 100 g of baker's yeast (*Saccharomyces cerevisiae*, SAF-Mannan, Biospringer) was heated at 80–85°C for 1 h in 1 l of NaOH (0.5 M) to hydrolyze the outer cell wall and intracellular components. This step was repeated after a water wash. Following centrifugation (15,000 *g* for 10 min), the resulting pellet was washed at least three times with water and three times with isopropanol. This yielded approximately 3–4 mg of purified, porous 2- to 4-μm, hollow β 1,3-d-glucan particles. One gram of empty β1,3-d-glucan particles resuspended in 100 ml of sodium carbonate buffer was then labeled with FITC by incubation with 10 mg of 5-(4,6-dichlorotriazinyl) amino fluorescein (DTAF) dissolved in 10 ml of ethanol for ∼16 h protected from light. Labeled GS were then washed at least five times in water. Wild-type mice fed an HFD for 8 weeks were first randomized according to their body weight and glucose tolerance. Mice were then treated with 12.5 mg/kg GeRPs loaded with siRNA (247 μg/kg) and Endoporter (2.27 mg/kg). Mice received six doses of fluorescently labeled GeRPs by intravenous injection over 15 days. For details concerning this experiment view part Methods and Supplementary Methods in (Tencerova, 2020).

Human liver spheroids and IGFBP7 administration

Cryopreserved primary human hepatocytes (Bioreclamation IVT) were cultured in 96-well ultra-low attachment plates (Corning) as previously described (Tencerova, 2020). Briefly, 1,500 cells/well were seeded in culture medium (Williams' medium E containing 11 mM glucose supplemented with 2 mM l-glutamine, 100 U/ml penicillin, 100 μg/ml streptomycin, 10 μg/ml insulin, 5.5 μg/ml transferrin, 6.7 ng/ml sodium selenite, and 100 nM dexamethasone) with 10% FBS as described previously. Following aggregation, cells were transitioned into serum-free Williams' medium E (PAN-Biotech) containing 5.5 mM glucose and 1 nM insulin for 7 days. On the day of the treatment, after 2 h of starvation, cells were exposed to recombinant human IGFBP7 (200 ng/ml; K95R, R&D Systems, 1334-B7-025 or wild type, R&D Systems, custom made) or insulin (100 nM) as reported previously (Tencerova, 2020). Protein was collected for immunoprecipitation assays and western blot analysis. Spheroid viability was controlled by ATP quantification using the CellTiter-Glo Luminescent Cell Viability Assay (Promega) with values normalized to the corresponding vehicle control on the same plate. No statistically significant differences in viability were observed between IGFBP7- and vehicle-treated controls when using heteroscedastic two-tailed *t*-tests ($n = 8$ spheroids) and $P < 0.05$ as the significance threshold (Morgantini *et al*, 2019). For analysis of lipoprotein production, the media were harvested and the level of LDL and VLDL was measured according to the manufacturer's protocol (Human Very Low-Density Lipoprotein [LDL] and Human

Very Low-Density Lipoprotein [VLDL] Elisa Kit, respectively; Abbexa).

Statistics

Box plots, heat maps, and donut graphs were generated in GraphPad Prism9 software. 2way ANOVA was used for multiple comparison testing, followed by Tukey's or Šídák's multiple comparisons tests. Ordinary one-way ANOVA followed by Dunnett's multiple comparisons test was used to compare the results with the corresponding control group. An unpaired t-test was used for pair reciprocal comparison of datasets. Bar plots display mean and standard deviation. The statistical significance of the test is depicted in plots by using the following GP code ($P < 0.05 = *$; $P < 0.001 = **$; $P < 0.0001 = ***$). Normality and homogeneity of variations were tested by the Anderson-Darling test, D'Agostino Pearson's test, and Shapiro–Wilk test. Data showing significant deviances from normal distribution was normalized by Log_2-transformation. For survival analyses, the data sets were compared by Log-rank and Grehan-Breslow Wilcoxon test. For complex differential analysis of omics data, we processed the data through an online platform for transcriptomic data analysis TCC (Sun *et al*, 2013)—based on the following R-packages (*edgeR, DESeq, baySeq*, and *NBPSeq*), iDep95 (Ge *et al*, 2018)—based on the following R-packages (*limma, DESeq2, GSEA, PAGE, GACE, RactomePA, Kallisto, Galaxy*) followed by subsequent analysis of assigned biological processes in Kegg pathways (www.genome.jp/kegg/pathway) and Flymine databases (https://www.flymine.org/flymine). An online platform for lipidomic data analysis (LipidSuite (Mohamed & Hill, 2021) – based on the R-package *lipidr*) was employed for differential comparison of obtained lipidomic datasets.

List of primers and other nucleotide sequences used in this work:

4EBP Forward: CCATGATCACCAGGAAGGTTGTCA	CG8846	FBgn0261560
4EBP Reverse: AGCCCGCTCGTAGATAAGTTTGGT	CG8846	FBgn0261560
EIF-4E Forward: AAGAAGAACATTCGCCCATG T	CG4035	FBgn0015218
EIF-4E Reverse: GGACTGCCGACGGAAACAAC	CG4035	FBgn0015218
MTP Forward: GAATCGAAATGCCCAGACG	CG9342	FBgn0266369
MTP Reverse: AACGTTGGTTTGTTTGAGAAGC	CG9342	FBgn0266369
HSL Forward: CAGTCCTACGAGATTCACGG	CG11055	FBgn0034491
HSL Reverse: GGCTTCGTTGGATAACATTGTG	CG11055	FBgn0034491
Bmm Forward: CACCGCGCCGCAATGAATGTATAA	CG5295	FBgn0036449
Bmm Reverse: TTCAATCACTGTTTGTCGGTCGGC	CG5295	FBgn0036449
apoLTP Forward: TGGGTGGATTGAAGCCACAG	CG15828	FBgn0032136
apoLTP Reverse: TGAGTGGATTTTCTCTCACTGC	CG15828	FBgn0032136
apoLPP Forward: TTGGAATCCTAGCTTCTGTGCT	CG11064	FBgn0087002
apoLPP Reverse: AGTCATAGTAGTTGCCGGGTAT	CG11064	FBgn0087002
Hif1a Forward: AGCCATCCATCTATGTGCC	CG45051	FBgn0266411
Hif1a Reverse: TCAAACGCCACGAGACGAC	CG45051	FBgn0266411
Nplp2 Forward: ATGGCCAAGCTCGCAATTTG	CG11051	FBgn0287423
Nplp2 Reverse: TCAACCTTCTTCGCGTCCAA	CG11051	FBgn0287423
Rp49 Forward: AAGCTGTCGCACAAATGGCG	CG7939	FBgn0002626
Rp49 Reverse: GCACGTTGTGCACCAGGAAC	CG7939	FBgn0002626
ImpL2 Forward: TTCGCGGTTTCTGGGCACCC	CG15009	FBgn0001257
ImpL2 Reverse: GCGCGTCCGATCGTCGCATA	CG15009	FBgn0001257
Dilp3 Forward: ACCAAAAAAGACCCGGCTCG	CG14167	FBgn0036046
Dilp3 Reverse: TGCAGCTCTGTCTTAACGCC	CG14167	FBgn0036046
Dilp6 Forward: CGG AAT ACG AAC AGA GAC GC	CG8167	FBgn0044047
Dilp6 Reverse: ACTGTTGGGAAATACATCGCC	CG8167	FBgn0044047
Upd3 Forward: AGAACACCTGCAATCTGAAGC	CG33542	FBgn0053542
Upd3 Reverse: TCTTGGTGCTCACTGTGGCC	CG33542	FBgn0053542
Egr Forward: AGCTGATCCCCCTGGTTTTG	CG12919	FBgn0033483
Egr Reverse: GCCAGATCGTTAGTGCGAGA	CG12919	FBgn0033483
Reg 1 Forward: GAGCAAATTGGACTCTACAGG	3L:4221582..4238579	

Reg 1 Reverse: GGGGAGCAACAAGTAACTCG	3L:4221582..4238579	
Reg 2 Forward: CTTTGGGCTGATAATTCCGG	3L:4221582..4238579	
Reg 2 Reverse: TACATATATCCATAGAACCACG	3L:4221582..4238579	
Reg 5 Forward: AGCCATCCATCTATGTGCC	3L:4221582..4238579	
Reg 5 Reverse: TCAAACGCCACGAGACGAC	3L:4221582..4238579	
Reg 7 Forward: GCAACTCAAATTCTTCAAACTCG	3L:4221582..4238579	
Reg 7 Reverse: TCGGACCACTTGCTTTGTGT	3L:4221582..4238579	
Reg 9 Forward: GAACCGTCGCCTTCCAG	3L:4221582..4238579	
Reg 9 Reverse: TGCCATGCCATTTGTTTCGC	3L:4221582..4238579	
Sam-S Forward: CAAATCAGCGACGCTATCTTGG	CG2674	FBgn0005278
Sam-S Reverse: TGTCTCACGAACAACCTTCTGG	CG2674	FBgn0005278
Human IGFBP7 Forward: GCCATCACCCAGGTCAGCAAG	GC04M057030	
Human IGFBP7 Reverse: GGATTCCGATGACCTCACAGCT	GC04M057030	
Human ACTB Forward: ATTGCCGACAGGATGCAGAA	GC07M005527	
Human ACTB Reverse: GCTGATCCACATCTGCTGGAA	GC07M005527	
Murine IGFBP7 Forward: TGCCCTCCATGAAATACCAC	ENSMUSG00000036256	
Murine IGFBP7 Reverse: GGCTGTCTGAGAGCACCTTT	ENSMUSG00000036256	
Murine Actb Forward: TCTACAATGAGCTGCGTGTGG	ENSMUSG00000029580	
Murine Actb Reverse: GTACATGGCTGGGGTGTTGAA	ENSMUSG00000029580	
Murine 36B4 Reverse: TCCAGGCTTTGGGCATCA	ENSMUSG00000067274	
Murine 36B4 Reverse: CTTTATCAGCTGCACATCACTCAGA	ENSMUSG00000067274	
IGFBP7-si 1 GCAAGAGGCGGAAGGGUAA	ENSMUSG00000036256	
IGFBP7-si 2 GGAGGACGCUGGAGAGUAU	ENSMUSG00000036256	
IGFBP7-si 3 AGGUGAAGGUGCUCAGUUA	ENSMUSG00000036256	

Genotypes of experimental models

Figure 1

(A–F) Hml>Gal4; TubGal80^{TS} x TRiP^{control} refers to $w^{1118}/+$; *Hml∆-Gal4/+; P{tubPGal80ts}/TRiP^{control}*
Hml>Gal4; TubGal80^{TS} x W^{control} corresponds to w^{1118}/w^{1118}; *Hml∆-Gal4/+; P{tubPGal80ts}/+*
(H, I) Crq>Gal4; UAS2xGFP x TRiP^{control} refers to $+/+$; $+/+$; *Crq-Gal4, UAS-2xeGFP/TRiP^{control}*
Crq>Gal4; UAS2xGFP x W^{control} corresponds to w^{1118}/w^{1118}; *Crq-Gal4, UAS-2xeGFP/+*

Figure 2

(A–C) Crq>Gal4; UAS-GFP corresponds to $+/+$; $+/+$; Crq-Gal4, UAS-2xeGFP/Crq-Gal4, UAS-2xeGFP
(D) ImpL2>mCherry corresponds to w^{1118}/w^{1118}; 20xUAS-6xmCherry/+; ImpL2-Gal4/+
(E) Crq>Gal4; UAS-GFP x W^{control} corresponds to w^{1118}/+; $+/+$; Crq-Gal4, UAS-2xeGFP/+
Crq>Gal4; UAS-GFP x Hif1α^{RNAi} corresponds to w^{1118}/+; $+/+$; UAS-Hif1α^{RNAi}/Crq-Gal4 UAS-2xeGFP
(F) Crq> Gal4; UAS-SimaGFP refers to w^{1118}/w^{1118}; +/PBac{sima-GFP.AC.FPTB}VK00037; Crq-Gal4 UAS-2xeGFP/+

Figure 3

(A–F) Hml>Gal4; TubGal80^{TS} x TRiP^{control} refers to $w^{1118}/+$; *Hml∆-Gal4/+; P{tubPGal80ts}/TRiP^{control}*
Hml>Gal4; TubGal80^{TS} x W^{control} corresponds to w^{1118}/w^{1118}; *Hml∆-Gal4/+; P{tubPGal80ts}/+*
Hml>Gal4; TubGal80^{TS} > ImpL2^{CDS} corresponds to w^{1118}/w^{1118}; *Hml∆-Gal4/+; P{tubPGal80ts}/UAS-ImpL2^{cds}*
Hml>Gal4; TubGal80^{TS} > ImpL2^{RNAi} corresponds to $w^{1118}/+$; *Hml∆-Gal4/UAS-ImpL2^{RNAi}; P{tubPGal80ts}/+*

Figure 4

(A) Hml>Gal4; TubGal80^{TS} x TRiP^{control} refers to $w^{1118}/+$; *Hml∆-Gal4/+; P{tubPGal80ts}/TRiP^{control}*
Hml>Gal4; TubGal80^{TS} x W^{control} corresponds to w^{1118}/w^{1118}; *Hml∆-Gal4/+; P{tubPGal80ts}/+*
Hml>Gal4; TubGal80^{TS} > ImpL2^{CDS} corresponds to w^{1118}/w^{1118}; *Hml∆-Gal4/+; P{tubPGal80ts}/UAS-ImpL2^{cds}*
Hml>Gal4; TubGal80^{TS} > ImpL2^{RNAi} corresponds to $w^{1118}/+$; *Hml∆-Gal4/UAS-ImpL2^{RNAi}; P{tubPGal80ts}/+*
(B–D) Hml>Gal4 TubGal80^{TS} x W^{control} corresponds to w^{1118}/w^{1118}; *Hml∆-Gal4 P{tubPGal80ts}/+; $+/+$*
Hml>Gal4 TubGal80^{TS} x ImpL2^{CDS} corresponds to w^{1118}/w^{1118}; *Hml∆-Gal4 P{tubPGal80ts}/+; UAS-ImpL2^{cds}/+*

Hml>Gal4 TubGal80^{TS} x foxo^{BG01018} ImpL2^{CDS} refers to w^{1118}/w^{1118}; *HmlΔ-Gal4 P{tubPGal80ts}/+; P{w[+mGT]=GT1} foxo^{BG01018} UAS-ImpL2^{cds}/+*

Figure 5

(A, B) Hml>Gal4 TubGal80^{TS}; tGPH-GFP x w^{1118} corresponds to w^{1118}/w^{1118}; *HmlΔ-Gal4 P{tubPGal80ts}/+; tGPH/+*
Hml>Gal4 TubGal80^{TS}; tGPH-GFP x ImpL2^{CDS} corresponds to w^{1118}/w^{1118}; *HmlΔ-Gal4 P{tubPGal80ts}/+; tGPH/UAS-ImpL2^{cds}*
Hml>Gal4 TubGal80^{TS}; tGPH-GFP x ImpL2^{RNAi} corresponds to w^{1118}/w^{1118}; *HmlΔ-Gal4 P{tubPGal80ts}/+; tGPH/ImpL2^{RNAi}*
(C, D) FB>Gal4 TubGal80^{TS} x W^{1118} corresponds to w^{1118}/+; *FB-Gal4/+; P{tubPGal80ts}/+*
FB>Gal4 TubGal80^{TS} x TRiP^{control} refers to +/+; *FB-Gal4/+; P{tubPGal80ts}/TRiP^{control}*
FB>Gal4 TubGal80^{TS} x InR^{CA} corresponds to +/+; *FB-Gal4/+; P{tubPGal80ts}/P{w[+mC]=UAS-InR.K1409A}3*
FB>Gal4 TubGal80^{TS} x InR^{DN} refers to +/+; *FB-Gal4/P{w[+mC]=UAS-InR.A1325D}2; P{tubPGal80ts}/+*
FB>Gal4 TubGal80^{TS} x PTEN^{CDS} corresponds to to +/+; *FB-Gal4/+; P{tubPGal80ts}/M{UAS-Pten.ORF.3xHA}ZH-86Fb*
Hml>Gal4 TubGal80^{TS} x foxo^{BG01018} ImpL2^{CDS} refers to w^{1118}/w^{1118}; *HmlΔ-Gal4 P{tubPGal80ts}/+; P{w[+mGT]=GT1} foxo^{BG01018} UAS-ImpL2^{cds}/+*
Hml>Gal4 TubGal80^{TS} x foxo^{BG01018} refers to w^{1118}/w^{1118}; *HmlΔ-Gal4 P{tubPGal80ts}/+; P{w[+mGT]=GT1}foxo^{BG01018}/P{w[+mGT]=GT1}foxo^{BG01018}*
(F, G) FB>Gal4 TubGal80^{TS} x TRiP^{control} refers to +/+; *FB-Gal4/+; P{tubPGal80ts}/TRiP^{control}*
FB>Gal4 TubGal80^{TS} x InR^{CA} corresponds to +/+; *FB-Gal4/+; P{tubPGal80ts}/P{w[+mC]=UAS-InR.K1409A}3*
FB>Gal4 TubGal80^{TS} x Mtp^{RNAi} refers to +/+; *FB-Gal4/P{y[+t7.7] v[+t1.8]=TRiP.HMC03446}attP40; P{tubPGal80ts}/+*
FB>Gal4 TubGal80^{TS} x apoLTP^{RNAi} refers to +/+; *FB-Gal4/+; P{tubPGal80ts}/P{y[+t7.7]v[+t1.8]=TRiP.HMC03294}attP2*
FB>Gal4 TubGal80^{TS} x apoLPP^{RNAi} corresponds to +/+; *FB-Gal4/+; P{tubPGal80ts}/P{y[+t7.7] v[+t1.8]=TRiP.HM05157}attP2*

Figure 6

(A-D) Crq>GFP x ImpL2^{RNAi} refers to w^{1118}/+; *UAS-ImpL2^{RNAi}/+; Crq-Gal4, UAS-2xeGFP/+*
Crq>GFP x ImpL2^{cds} corresponds to w^{1118}/w^{1118}; +/+; Crq-Gal4, UAS-2xeGFP/UAS-ImpL2^{cds}
Crq>GFP x TRiP^{control} refers to +/+; +/+; Crq-Gal4, UAS-2xeGFP/TRiP^{control}
Crq>GFP x W^{1118} corresponds to w^{1118}/w^{1118}; Crq-Gal4, UAS-2xeGFP/+
(E-F) Hml>Gal4; TubGal80^{TS} x TRiP^{control} refers to w^{1118}/+; HmlΔ-Gal4/+; P{tubPGal80ts}/TRiP^{control}
Hml>Gal4; TubGal80^{TS} x W^{control} corresponds to w^{1118}/w^{1118}; HmlΔ-Gal4/+; P{tubPGal80ts}/+
Hml>Gal4; TubGal80^{TS} x ImpL2^{CDS} corresponds to w^{1118}/w^{1118}; HmlΔ-Gal4/+; P{tubPGal80ts}/UAS-ImpL2^{cds}
Hml>Gal4; TubGal80^{TS} x ImpL2^{RNAi} corresponds to w^{1118}/+; HmlΔ-Gal4/UAS-ImpL2^{RNAi}; P{tubPGal80ts}/+

Figure 7

(A) FB>Gal4 TubGal80^{TS} x LPP^{RNAi} corresponds to +/+; FB-Gal4/+; P{tubPGal80ts}/P{y[+t7.7] v[+t1.8]=TRiP.HM05157}attP2
W^{control} x FB>Gal4 TubGal80^{TS} corresponds to w^{1118}/+; FB-Gal4/+; P{tubPGal80ts}/+
LPP^{RNAi} x W^{control} corresponds to w^{1118}/+; +/+; +/P{y[+t7.7] v[+t1.8]=TRiP.HM05157}attP2
(B–D) FB>Gal4 TubGal80^{TS} x LPP^{RNAi} corresponds to +/+; FB-Gal4/+; P{tubPGal80ts}/P{y[+t7.7] v[+t1.8]=TRiP.HM05157}attP2
W^{control} x FB>Gal4 TubGal80^{TS} corresponds to w^{1118}/+; FB-Gal4/+; P{tubPGal80ts}/+
(E, F) Crq>Gal4; UAS-GFP corresponds to +/+; +/+; Crq-Gal4, UAS-2xeGFP/Crq-Gal4, UAS-2xeGFP

Data availability

The datasets produced in this study are available in the following databases:
RNA-Seq data: Gene Expression Omnibus; GSE237617 (https://www.ncbi.nlm.nih.gov/geo/query/acc.cgi?acc=GSE237617).
Lipidomic data: DRYAD; DOI: 10.5061/dryad.9zw3r22kw.

Expanded View for this article is available online.

Author contributions
Gabriela Krejčová: Conceptualization; resources; data curation; formal analysis; supervision; funding acquisition; validation; investigation; visualization; methodology; writing – original draft; project administration;

Disclosure and competing interests statement

The authors declare that they have no conflict of interest.

References

Akhtar DH, Iqbal U, Vazquez-Montesino LM, Dennis BB, Ahmed A (2019) Pathogenesis of insulin resistance and atherogenic dyslipidemia in nonalcoholic fatty liver disease. *J Clin Transl Hepatol* 7: 1–9

Al-Mansoori L, Al-Jaber H, Prince MS, Elrayess MA (2022) Role of inflammatory cytokines, growth factors and adipokines in adipogenesis and insulin resistance. *Inflammation* 45: 31–44

Arrese EL, Canavoso LE, Jouni ZE, Pennington JE, Tsuchida K, Wells MA (2001) Lipid storage and mobilization in insects: current status and future directions. *Insect Biochem Mol Biol* 31: 7–17

Bajgar A, Dolezal T (2018) Extracellular adenosine modulates host-pathogen interactions through regulation of systemic metabolism during immune response in Drosophila. *PLoS Pathog* 14: e1007022

Bayley JS, Sørensen JG, Moos M, Koštál V, Overgaard J (2020) Cold acclimation increases depolarization resistance and tolerance in muscle fibers from a chill-susceptible insect, *Locusta migratoria. Am J Physiol Integr Comp Physiol* 319: R439–R447

Bell CC, Lauschke VM, Vorrink SU, Palmgren H, Duffin R, Andersson TB, Ingelman-Sundberg M (2017) Transcriptional, functional, and mechanistic comparisons of stem cell–derived hepatocytes, HepaRG cells, and three-dimensional human hepatocyte spheroids as predictive *in vitro* systems for drug-induced liver injury. *Drug Metab Dispos* 45: 419–429

Brankatschk M, Dunst S, Nemetschke L, Eaton S (2014) Delivery of circulating lipoproteins to specific neurons in the Drosophila brain regulates systemic insulin signaling. *Elife* 3: e02862

Britton JS, Lockwood WK, Li L, Cohen SM, Edgar BA (2002) Drosophila's insulin/PI3-kinase pathway coordinates cellular metabolism with nutritional conditions. *Dev Cell* 2: 239–249

Canavoso LE, Yun HK, Jouni ZE, Wells MA (2004) Lipid transfer particle mediates the delivery of diacylglycerol from lipophorin to fat body in larval *Manduca sexta. J Lipid Res* 45: 456–465

Chi H (2022) Immunometabolism at the intersection of metabolic signaling, cell fate, and systems immunology. *Cell Mol Immunol* 19: 299–302

Chow A, Brown BD, Merad M (2011) Studying the mononuclear phagocyte system in the molecular age. *Nat Rev Immunol* 11: 788–798

Corcoran SE, O'Neill LAJ (2016) HIF1α and metabolic reprogramming in inflammation. *J Clin Invest* 126: 3699–3707

DiAngelo JR, Bland ML, Bambina S, Cherry S, Birnbaum MJ (2009) The immune response attenuates growth and nutrient storage in *Drosophila* by reducing insulin signaling. *Proc Natl Acad Sci USA* 106: 20853–20858

Dionne MS, Schneider DS (2008) Models of infectious diseases in the fruit fly *Drosophila melanogaster. Dis Model Mech* 1: 43–49

Figueroa-Clarevega A, Bilder D (2015) Malignant *Drosophila* tumors interrupt insulin signaling to induce cachexia-like wasting. *Dev Cell* 33: 47–55

Galvan-Pena S, O'Neill LAJ (2014) Metabolic reprograming in macrophage polarization. *Front Immunol* 5: 420

Ganeshan K, Chawla A (2014) Metabolic regulation of immune responses. *Annu Rev Immunol* 32: 609–634

Ganeshan K, Nikkanen J, Man K, Leong YA, Sogawa Y, Maschek JA, Van Ry T, Chagwedera DN, Cox JE, Chawla A (2019) Energetic trade-offs and hypometabolic states promote disease tolerance. *Cell* 177: 399–413.e12

Ge SX, Son EW, Yao R (2018) iDEP: an integrated web application for differential expression and pathway analysis of RNA-Seq data. *BMC Bioinformatics* 19: 534

Grönke S, Beller M, Fellert S, Ramakrishnan H, Jäckle H, Kühnlein RP (2003) Control of fat storage by a *Drosophila* PAT domain protein. *Curr Biol* 13: 603–606

Hang S, Purdy AE, Robins WP, Wang Z, Mandal M, Chang S, Mekalanos JJ, Watnick PI (2014) The acetate switch of an intestinal pathogen disrupts host insulin signaling and lipid metabolism. *Cell Host Microbe* 16: 592–604

Honegger B, Galic M, Köhler K, Wittwer F, Brogiolo W, Hafen E, Stocker H (2008) Imp-L2, a putative homolog of vertebrate IGF-binding protein 7, counteracts insulin signaling in *Drosophila* and is essential for starvation resistance. *J Biol* 7: 10

Izquierdo MC, Shanmugarajah N, Lee SX, Kraakman MJ, Westerterp M, Kitamoto T, Harris M, Cook JR, Gusarova GA, Zhong K *et al* (2022) Hepatic FoxOs link insulin signaling with plasma lipoprotein metabolism through an apolipoprotein M/sphingosine-1-phosphate pathway. *J Clin Invest* 132: e146219

Kedia-Mehta N, Finlay DK (2019) Competition for nutrients and its role in controlling immune responses. *Nat Commun* 10: 2123

Koyama T, Rodrigues MA, Athanasiadis A, Shingleton AW, Mirth CK (2014) Nutritional control of body size through FoxO-Ultraspiracle mediated ecdysone biosynthesis. *Elife* 3: e03091

Krejčová G, Danielová A, Nedbalová P, Kazek M, Strych L, Chawla G, Tennessen JM, Lieskovská J, Jindra M, Doležal T *et al* (2019) *Drosophila* macrophages switch to aerobic glycolysis to mount effective antibacterial defense. *Elife* 8: e50414

Kurucz É, Márkus R, Zsámboki J, Folkl-Medzihradszky K, Darula Z, Vilmos P, Udvardy A, Krausz I, Lukacsovich T, Gateff E *et al* (2007) Nimrod, a putative phagocytosis receptor with EGF repeats in *Drosophila* plasmatocytes. *Curr Biol* 17: 649–654

Kwon Y, Song W, Droujinine IA, Hu Y, Asara JM, Perrimon N (2015) Systemic organ wasting induced by localized expression of the secreted insulin/IGF antagonist ImpL2. *Dev Cell* 33: 36–46

Lee H-J, Hong W-G, Woo Y, Ahn J-H, Ko H-J, Kim H, Moon S, Hahn T-W, Jung YM, Song D-K *et al* (2020) Lysophosphatidylcholine enhances bactericidal activity by promoting phagosome maturation via the activation of the NF-κB pathway during *Salmonella* infection in mouse macrophages. *Mol Cells* 43: 989–1001

Liu P, Zhu W, Chen C, Yan B, Zhu L, Chen X, Peng C (2020) The mechanisms of lysophosphatidylcholine in the development of diseases. *Life Sci* 247: 117443

Martínez BA, Hoyle RG, Yeudall S, Granade ME, Harris TE, Castle JD, Leitinger N, Bland ML (2020) Innate immune signaling in *Drosophila* shifts anabolic

lipid metabolism from triglyceride storage to phospholipid synthesis to support immune function. *PLoS Genet* 16: e1009192

Mills CD, Kincaid K, Alt JM, Heilman MJ, Hill AM (2000) M-1/M-2 macrophages and the Th1/Th2 paradigm. *J Immunol* 164: 6166–6173

Mohamed A, Hill MM (2021) LipidSuite: interactive web server for lipidomics differential and enrichment analysis. *Nucleic Acids Res* 49: W346–W351

Morgantini C, Jager J, Li X, Levi L, Azzimato V, Sulen A, Barreby E, Xu C, Tencerova M, Näslund E *et al* (2019) Liver macrophages regulate systemic metabolism through non-inflammatory factors. *Nat Metab* 1: 445–459

Newsholme P (2021) Cellular and metabolic mechanisms of nutrient actions in immune function. *Nutr Diabetes* 11: 22

Oliva-Vilarnau N, Vorrink SU, Ingelman-Sundberg M, Lauschke VM (2020) A 3D cell culture model identifies Wnt/β-catenin mediated inhibition of p53 as a critical step during human hepatocyte regeneration. *Adv Sci* 7: 2000248

Owusu-Ansah E, Song W, Perrimon N (2013) Muscle mitohormesis promotes longevity via systemic repression of insulin signaling. *Cell* 155: 699–712

Palm W, Sampaio JL, Brankatschk M, Carvalho M, Mahmoud A, Shevchenko A, Eaton S (2012) Lipoproteins in *Drosophila melanogaster*—assembly, function, and influence on tissue lipid composition. *PLoS Genet* 8: e1002828

Rankin LC, Artis D (2018) Beyond host defense: emerging functions of the immune system in regulating complex tissue physiology. *Cell* 173: 554–567

Remmerie A, Scott CL (2018) Macrophages and lipid metabolism. *Cell Immunol* 330: 27–42

Roed NK, Viola CM, Kristensen O, Schluckebier G, Norrman M, Sajid W, Wade JD, Andersen AS, Kristensen C, Ganderton TR *et al* (2018) Structures of insect Imp-L2 suggest an alternative strategy for regulating the bioavailability of insulin-like hormones. *Nat Commun* 9: 3860

Santalla M, García A, Mattiazzi A, Valverde CA, Schiemann R, Paululat A, Hernández G, Meyer H, Ferrero P (2022) Interplay between SERCA, 4E-BP, and eIF4E in the *Drosophila* heart. *PloS One* 17: e0267156

Sloth Andersen A, Hertz Hansen P, Schäffer L, Kristensen C (2000) A new secreted insect protein belonging to the immunoglobulin superfamily binds insulin and related peptides and inhibits their activities. *J Biol Chem* 275: 16948–16953

Sun J, Nishiyama T, Shimizu K, Kadota K (2013) TCC: an R package for comparing tag count data with robust normalization strategies. *BMC Bioinformatics* 14: 219

Tencerova M (2020) Glucan-encapsulated siRNA particles (GeRPs) for specific gene silencing in Kupffer cells in mouse liver. *Methods Mol Biol* 2164: 65–73

Tencerova M, Aouadi M, Vangala P, Nicoloro SM, Yawe JC, Cohen JL, Shen Y, Garcia-Menendez L, Pedersen DJ, Gallagher-Dorval K *et al* (2015) Activated Kupffer cells inhibit insulin sensitivity in obese mice. *FASEB J* 29: 2959–2969

Tesz GJ, Aouadi M, Prot M, Nicoloro SM, Boutet E, Amano SU, Goller A, Wang M, Guo C-A, Salomon WE *et al* (2011) Glucan particles for selective delivery of siRNA to phagocytic cells in mice. *Biochem J* 436: 351–362

Tsatsoulis A, Mantzaris MD, Bellou S, Andrikoula M (2013) Insulin resistance: an adaptive mechanism becomes maladaptive in the current environment — An evolutionary perspective. *Metabolism* 62: 622–633

Vorrink SU, Ullah S, Schmidt S, Nandania J, Velagapudi V, Beck O, Ingelman-Sundberg M, Lauschke VM (2017) Endogenous and xenobiotic metabolic stability of primary human hepatocytes in long-term 3D spheroid cultures revealed by a combination of targeted and untargeted metabolomics. *FASEB J* 31: 2696–2708

Wasyluk W, Zwolak A (2021) Metabolic alterations in sepsis. *J Clin Med* 10: 2412

Yan J, Horng T (2020) Lipid metabolism in regulation of macrophage functions. *Trends Cell Biol* 30: 979–989

Zhao X, Karpac J (2021) Glutamate metabolism directs energetic trade-offs to shape host-pathogen susceptibility in *Drosophila*. *Cell Metab* 33: 2428–2444.e8

Zhao P, Huang P, Xu T, Xiang X, Sun Y, Liu J, Yan C, Wang L, Gao J, Cui S *et al* (2021) Fat body Ire1 regulates lipid homeostasis through the Xbp1s-FoxO axis in *Drosophila*. *iScience* 24: 102819